Mineralium Deposita (2024) 59:23–46
https://doi.org/10.1007/s00126-023-01198-4

ARTICLE

Origin and tectonic environment of the Longbohe Fe-Cu-(LREE) deposit in the Ailao Shan–Red River shear zone, Southwest China: a Neoproterozoic subduction-related IOCG deposit?

Lei Liu[1,2] · Wei Terry Chen[1,2] · Xiao-Chun Li[2,3] · Xin-Fu Zhao[4,5]

Received: 13 February 2023 / Accepted: 25 July 2023 / Published online: 4 August 2023

Abstract

The Longbohe Fe-Cu-(LREE) deposit in the Longbohe–Sin Quyen (LSQ) Fe-Cu belt in the border zone of South China and northern Vietnam has a resource of > 1 million tonnes Cu, and was once speculated to be a potentially important subduction-related deposit of Precambrian age, but with poor constraints. Our study reveals that the major Fe-, Cu-, and LREE mineralization comprises three stages and are comparable to typical IOCG deposits worldwide. Stage I is characterized by pervasive Na alteration, followed by Fe mineralization stage (Stage II) consisting of Ti-poor magnetite associated with Ca-Na alteration forming amphibole and albite. Stage III, the Cu-LREE mineralization stage, is composed mainly of chalcopyrite and REE-rich allanite with minor pyrrhotite and pyrite. Stages I and II formed at broadly comparable temperatures of 515 to 670 ºC, and have $\delta^{18}O$ fluid values of 4.3 to 11.7 ‰, indicating dominantly magmatic fluids. Furthermore, they have hydrothermal zircon with $\varepsilon_{Hf(t)}$ values (7.5 to 12.7) similar to coeval mafic intrusions in the region, likely indicating a mafic magma-source for the fluids. Stage III fluids have lower temperatures (332 to 402 ºC) but exhibit magmatic-like $\delta^{34}S$ values (1.2 to 3.7 ‰) similarly suggestive of a major magmatic source. However, they have distinctly lower $\varepsilon_{Hf(t)}$ and $\varepsilon_{Nd(t)}$ values comparable to those of coeval regional felsic intrusions, suggesting that an additional component of REE-rich external fluid from felsic magmas was involved during the Cu-REE mineralization. Hydrothermal zircons from Stages II and III have similar U–Pb ages of ~ 850 Ma, providing tight constraints on the timing of Fe-Cu mineralization. The new U–Pb ages indicate that the Longbohe deposit is coeval with the Sin Quyen IOCG deposit in northern Vietnam, and with the regional subduction-related magmatism, indicating that the Longbohe–Sin Quyen belt is of Neoproterozoic age and formed in a convergent setting.

Keywords Longbohe deposit · C-O-S-Hf isotopes · Zircon U–Pb dating · Subduction-related · IOCG deposits

Introduction

Since the discovery of the world-class Olympic Dam deposit in 1975 and the definition of the iron oxide copper–gold (IOCG) clan by Hitzman et al. (1992), similar deposits have been important targets of exploration and academic research. This type of deposit has been proved to be an important source of Fe, Cu, and Au in the past decades (Hitzman et al. 1992; Hitzman and Valenta 2005; Williams et al. 2005; Groves et al. 2010), and also documented to be enriched in REE and Co (Mudd et al. 2013; Weng et al. 2015). Previous studies indicated that IOCG deposits mainly formed in the intra-continental environments, particularly in the Precambrian, whereas examples from convergent settings were mostly Phanerozoic in ages (e.g., Mesozoic Andes IOCG belt) (Hitzman 2000; Groves et al. 2010). Some researchers, for example, Groves et al. (2010) speculated

Editorial handling: R. Hu

✉ Wei Terry Chen
chenwei@mail.gyig.ac.cn

1 State Key Laboratory of Ore Deposit Geochemistry, Institute of Geochemistry, Chinese Academy of Sciences, Guiyang 550081, China

2 College of Earth and Planetary Sciences, University of Chinese Academy of Sciences, Beijing 100049, China

3 Key Laboratory of Mineral Resources, Institute of Geology and Geophysics, Chinese Academy of Sciences, Beijing 100029, China

4 State Key Laboratory of Geological Processes and Mineral Resources, China University of Geosciences, Wuhan 430074, China

5 School of Earth Resources, China University of Geosciences, Wuhan 430074, China

that Precambrian IOCG deposits forming in convergent settings will be found in future, if the similar lithospheric conditions at where the Phanerozoic deposits formed could be identified in the Precambrian. However, whether convergent setting-related IOCGs are common in Precambrian is still an open end question. Moreover, the characteristics, genesis, and uniqueness (when compared to Precambrian intra-continental and Phanerozoic subduction-related ones) are still poorly understood. Therefore, identifying and characterizing Precambrian IOCG variants from convergent settings would be important to understanding of the IOCG clan and impact directly on the exploration strategy.

A number of Fe-Cu deposits and prospects are distributed along the ASRR shear zone in South Yunnan, China and northern Vietnam; they define a potentially important Fe-Cu belt (Fig. 1b; Li and Zhou 2018; Liu and Chen 2019). Representative examples include the Longbohe deposit in southwestern Yunnan, China and the Sin Quyen deposit in northern Vietnam (Fig. 1c), and thus this belt was known as the Longbohe–Sin Quyen (LSQ) Fe-Cu belt (Liu and Chen 2019). The potential resources of the LSQ Fe-Cu belt were estimated to be > 1.5 Mt Cu, > 0.3 Mt REE, and > 30 t Au (Cui 2007; Duong et al. 2021). Despite its economically significance, this Fe-Cu belt received little attention in the past and with the only existing few studies in the literature on the Sin Quyen deposit in northern Vietnam (e.g., McLean 2001; Li and Zhou 2018; Li et al. 2018a, c; Ngo et al. 2020; Duong et al. 2021). These studies have shown that the Sin Quyen deposit has mineralization styles comparable to typical IOCG deposits worldwide, and is coeval with the Neoproterozoic (~ 840 Ma) subduction-related magmatism in the region (Cai et al. 2014, 2015; Wang et al. 2016; Li et al. 2018b). These studies hence suggested that the Sin Quyen deposit was likely a IOCG deposit which formed in a convergent setting, thus raising the possibility that the LSQ belt is a potentially Precambrian IOCG belt related to subduction at that time. However, it is currently unclear if other deposits in the LSQ belt have similar mineralization styles and formed at the same mineralizing event, due to limited constraints on the mineralization style and age of these deposits.

In this study, we conducted an investigation on the Longbohe deposit which is another large-scale Fe-Cu deposit in the LSQ Fe-Cu belt. We described the geology and alteration/mineralization styles of the deposit, in order to establish

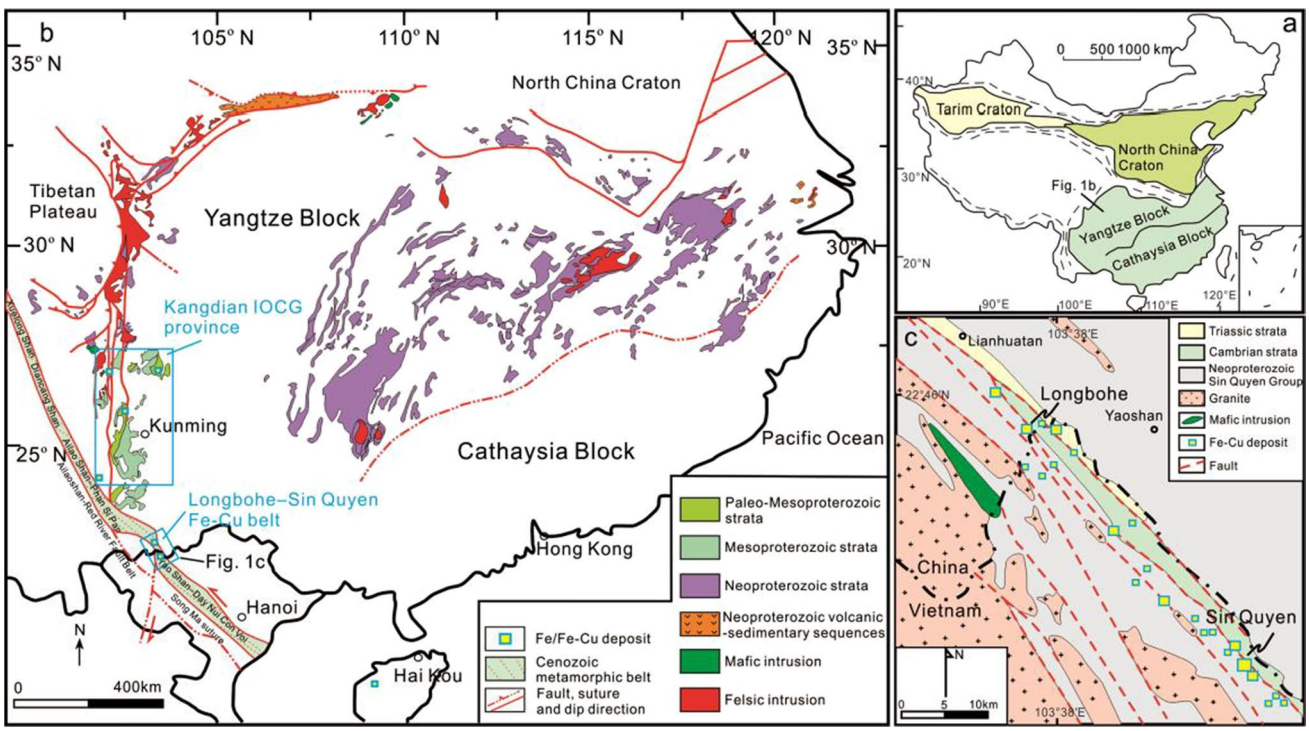

Fig. 1 **a** Simplified tectonic map of China (modified after Zhao and Cawood 2012). **b** Simplified geological map showing the distribution of major Proterozoic strata and Neoproterozoic igneous rocks of the Yangtze Block (after Zhou et al. 2014). **c** Simplified geological map displaying distribution of Fe-Cu deposits along the Ailao Shan–Red River shear zone between South China and northern Vietnam (after Zhou et al. 2014)

a paragenetic sequence for a comprehensive comparison with the Sin Quyen deposit and other typical IOCG deposits worldwide. LA-ICPMS U–Pb ages of hydrothermal zircon in the Fe and Cu ores tightly constrain the timing and tectonic setting of the mineralization. Stable isotopes (C, O and S) and Hf isotope data on hydrothermal zircon further allow us to determine the origin and evolution of the ore-forming fluids, and to establish an ore-forming model for the Longbohe deposit. A comprehensive comparison of the LSQ belt with other IOCG belts in different settings, in terms of alteration/mineralization, metal associations and fluid sources, was also made. The new findings have important implications for the regional Fe-Cu metallogeny in the ASRR shear zone and for the understanding of the diversity of IOCG systems.

Regional geology

Ailao Shan–Red River (ASRR) shear zone

South China consists of the Yangtze Block to the northwest and the Cathaysia Block to the southeast, which amalgamated at ~ 830 Ma along the Jiangnan orogenic belt (Fig. 1a, b; Zhao and Cawood 2012). The South China Block is separated from the North China Craton by the Qinling–Sulu–Dabie orogenic belt to the north, and from the Tibetan Plateau by the Songpan–Gantze terrane to the west (Fig. 1b). The boundary between the South China and Indochina Block was inferred to be the ASRR shear zone (Tapponnier et al. 1990; Leloup et al. 1995) or Song Ma belt (Chung et al. 1997; Faure et al. 2014).

The ASRR shear zone is a left-lateral continental strike-slip fault and extends over 1000 km from southeastern Tibet to the Gulf of Tonkin and the South China Sea (Fig. 1b; Chung et al. 1997; Searle 2006; Searle et al. 2010), with southeastward displacement of the Indochina Block relative to South China of at least 500 km (Tapponnier et al. 1990; Leloup and Kienast 1993; Leloup et al. 1995). The shear zone represents the most prominent geological discontinuity in Southeast Asia and consists of four main metamorphic units, namely Xuelong Shan, Diancang Shan, Ailao Shan–Phan Si Pan and Yao Shan–Day Nui Con Voi from northwest to southeast (Chung et al. 1997; Wu 2012; Weng 2014). The Ailao Shan–Phan Si Pan unit where the Longbohe–Sin Quyen Fe-Cu belt is located reaches from Yunnan province of China to northern Vietnam.

In the Ailao Shan–Phan Si Pan unit, the currently documented Proterozoic metamorphic basements include the Ailaoshan and Longbohe Groups in SW China and the Suoi Chieng Formation and Sin Quyen Group in NW Vietnam. The Ailaoshan Group mainly comprises amphibolites, gneiss, schist, phyllite and slate with minor granulite, migmatite and marble, which were metamorphosed under greenschist to amphibolite facies conditions (Zhai et al. 1990; Li et al. 2008, 2009; Wang et al. 2013; Gong and Jiang 2017; Ji et al. 2017). The Longbohe Group includes meta-volcanic and meta-sedimentary rocks, and is in fault contact with the Ailaoshan Group in the southwest (Fig. 2a; Liu et al. 2005; Liu and Chen 2019). The Suoi Chieng Formation mainly consists of granitic gneiss, biotite-amphibole gneiss, biotite schist and amphibolite, conformably overlain by the Sin Quyen Group (Tran 2011). The Sin Quyen Group is composed of mica schist, graphite schist, gneiss and minor marble (Hieu et al. 2010, 2012). Zircon U–Pb geochronology has shown that the so-called "volcanic-sedimentary sequences" of the Longbohe Group consist of at least two units which formed in the late Paleoproterozoic (~ 1700 Ma) and Neoproterozoic (loosely constrained at ~ 1000 Ma), respectively, whereas the meta-sedimentary rocks of the Sin Quyen Group were deposited at ~ 870 Ma (Hieu et al. 2012; Liu and Chen 2019).

Abundant Neoproterozoic (~ 850 to ~ 740 Ma) igneous rocks have been identified in the Ailao Shan–Phan Si Pan belt (e.g., Hieu et al. 2009; Cai et al. 2014, 2015; Wang et al. 2016; Chen et al. 2017; Li et al. 2018b). These intrusions have geochemical signatures of arc affinity and are considered to have formed in a subduction-related setting (e.g., Qi et al. 2012, 2014, 2016; Cai et al. 2014, 2015; Wang et al. 2016; Li et al. 2018b). They are thought be part of a giant arc system of the western Yangtze Block which became displaced into the ASRR shear zone during the Cenozoic (e.g., Hieu et al. 2009; Cai et al. 2014, 2015; Li et al. 2018b). Previous studies also identified some felsic intrusions of 259–249 Ma in the belt, and which are likely genetically linked to the Emeishan Large Igneous Province (Usuki et al. 2015). In addition, the Cenozoic (~ 30 Ma) activation of the ASRR shear zone produced numerous Cenozoic magmatic rocks in the Ailao Shan–Phan Si Pan belt (e.g., Cao et al. 2011; Liu et al. 2012, 2015).

Longbohe–Sin Quyen Fe-Cu belt

In addition to the well-known and large deposits of Longbohe in southwest China and Sin Quyen in northern Vietnam, there are other deposits/prospects, such as Nam Chac, Soui Thau, Pin Ngan Chai and Lung Thang, but their resources are relatively small (McLean 2001; Li and Zhou 2018). These deposits form a metallogenic Fe-Cu belt extending from Yunnan province, South China to northern Vietnam, namely the

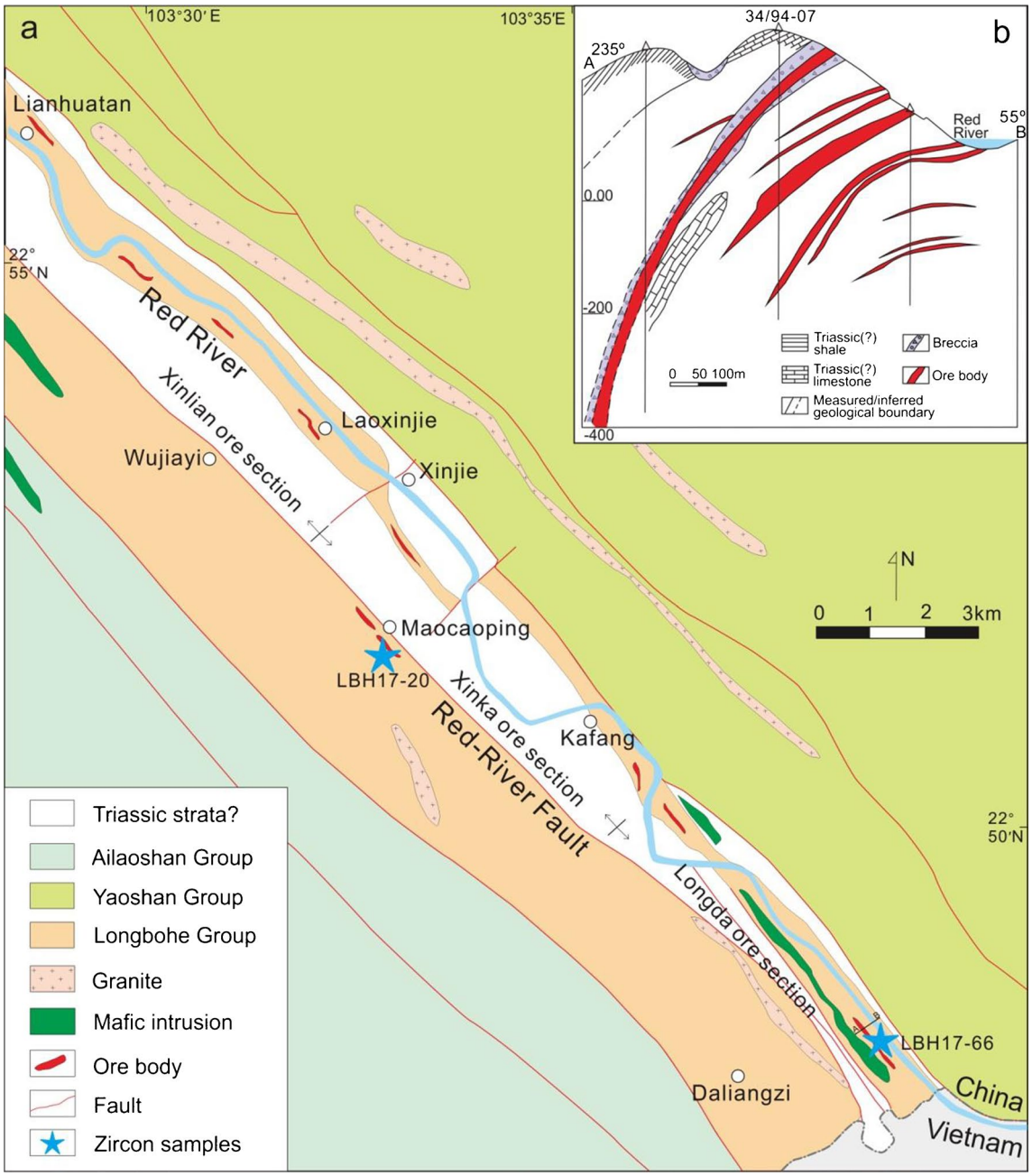

Fig. 2 **a** Simplified geological map of the Longbohe deposit (modified from Cui 2007). **b** Cross section of No. 34 located in the Longda ore section of the Longbohe mine (modified from Cui 2007)

Longbohe–Sin Quyen (LSQ) Fe-Cu belt (e.g., Li and Zhou 2018; Liu and Chen 2019). The ore bodies of this belt are similarly hosted in meta-sedimentary and meta-volcanic rocks of the Proterozoic Longbohe and Sin Quyen Groups that are variably metamorphosed or foliated. In the past decades, a number of studies on this belt are available but mostly focused on the Sin Quyen deposit (e.g., McLean 2001; Li and Zhou 2018; Li et al. 2018a, c; Ngo et al. 2020; Duong et al. 2021). It was documented that the Sin Quyen deposit, forming at 840 Ma, has a paragenetic sequence including pre-ore Na alteration and early Fe mineralization

(magnetite), followed by Cu-(Au) mineralization (chalcopyrite); these features are similar to typical IOCG deposits worldwide (e.g., McLean 2001; Li and Zhou 2018; Li et al. 2018a). As such, the LSQ Fe-Cu belt was suggested to be likely an IOCG metallogenic belt which was once considered to be part of the Kangdian IOCG province before being displaced into the ASRR shear zone (Fig. 1b; Zhou et al. 2014; Liu and Chen 2019; Chen et al. 2022). However, it is notable that the major mineralization events in the Kangdian IOCG province were documented at ~ 1660 and ~ 1080 Ma (e.g., Chen and Zhou 2012; Zhao et al. 2013, 2017), significantly older than the Sin Quyen deposit.

Geology of the Longbohe deposit

Occurrence of ore bodies

Early exploration in the Longbohe deposit revealed an estimated resource of ~ 1 Mt Cu with an average grade of ~ 0.91 wt% (Cui 2007). The ore bodies of this deposit are mainly hosted in the meta-volcanic and meta-sedimentary rocks (e.g., schist) of the Proterozoic Longbohe Group. They comprise the Xinlian, Xinka and Longda ore sections from northwest to southeast (Fig. 2a), and are mostly as stratabound and/or in irregular lenses that are structurally controlled. They are striking NW–SE

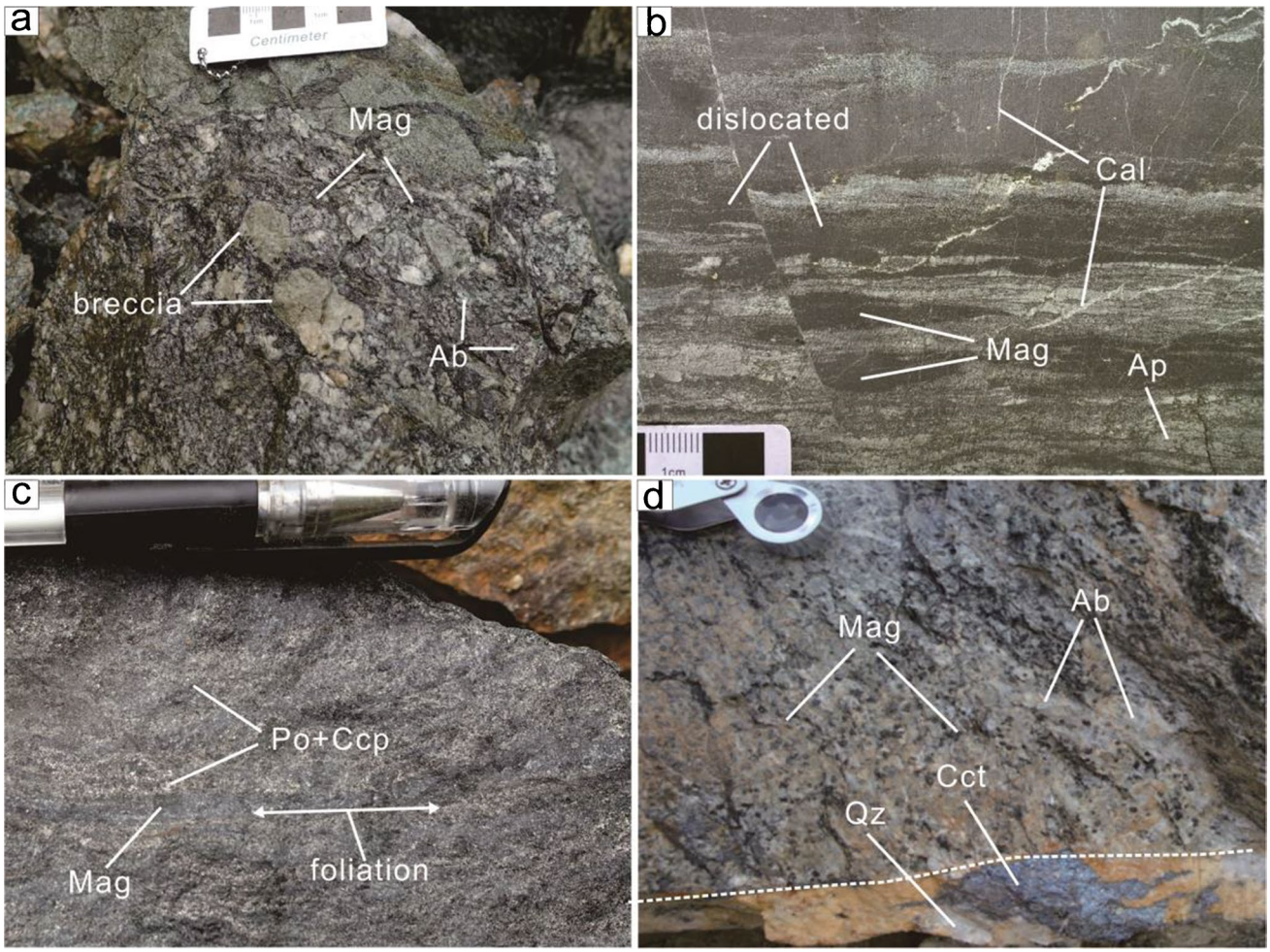

Fig. 3 **a** Brecciated ore showing that breccias of country rock were cemented by matrix dominated by magnetite and albite. **b** Dislocation and foliation of the massive Fe ore, indicative of strong deformation. **c** Banded magnetite-sulfide ore showing that early magnetite was overprinted by sulfides. **d** Disseminated Fe ore crosscut by late undeformed sulfide vein. Ab: albite, Ap: apatite, Cal: calcite, Ccp: chalcopyrite, Cct: chalcocite, Mag: magnetite, Po: pyrrhotite, Qz: quartz

and dipping to the southwest, with generally dozens to hundreds of meters in length, up to dozens of meters in width and dozens to hundreds of meters in extent along dip (Fig. 2b; Cui 2007). Both the country rocks and the ore bodies are deformed, locally manifested by fractures and dislocated and banded structures (Fig. 3a, b, c).

Mineralization styles

There is no obvious metal zonation at deposit scale, but the ores can be divided into oxide and oxide-sulfide types in term of relative proportion of iron oxides and Cu-sulfides. The oxide ores, have massive, banded, or disseminated structures (Fig. 3), and are composed mainly of magnetite with subordinate albite, amphibole, chlorite, and apatite with minor or without sulfides. In mixed oxide-sulfide ores, sulfide minerals are dominated by chalcopyrite, pyrrhotite and pyrite that occur generally as pervasive or banded replacements overprinting early magnetite-rich components. Both oxide and oxide-sulfide ores are variably deformed, manifested by lineation of minerals (Fig. 3c), and are locally crosscut by abundant sulfide veins that are not deformed (Fig. 3d). These veins are mainly composed of variable amounts of chalcopyrite, bornite, chalcocite, quartz, and carbonate minerals.

Paragenetic sequence of alteration and mineralization

Based on macro- and micro-textural relationships of mineral assemblages, four main stages of alteration and mineralization have been established for the Longbohe Fe-Cu-(LREE) deposit (Fig. 4). The chemical data of minerals are listed in ESM Table 1.

Stage I: Na-(Fe) alteration

The pre-ore Na-(Fe) alteration is generally characterized by abundant albite and minor magnetite, pervasively replacing the country rock. Albite is usually euhedral to subhedral or granular in shapes, and crosscut by late calcite veinlets (Fig. 5a). Albite has pure end-member compositions with Na/(Na + Ca + K) ratios close to 1.00. Magnetite is generally fine-grained and granular in shapes (Fig. 5a). Under BSE images, both albite and magnetite are homogeneous without clear sign of late modification (Fig. 5e). In addition, minor titanite and epidote is locally present in the albitized rocks

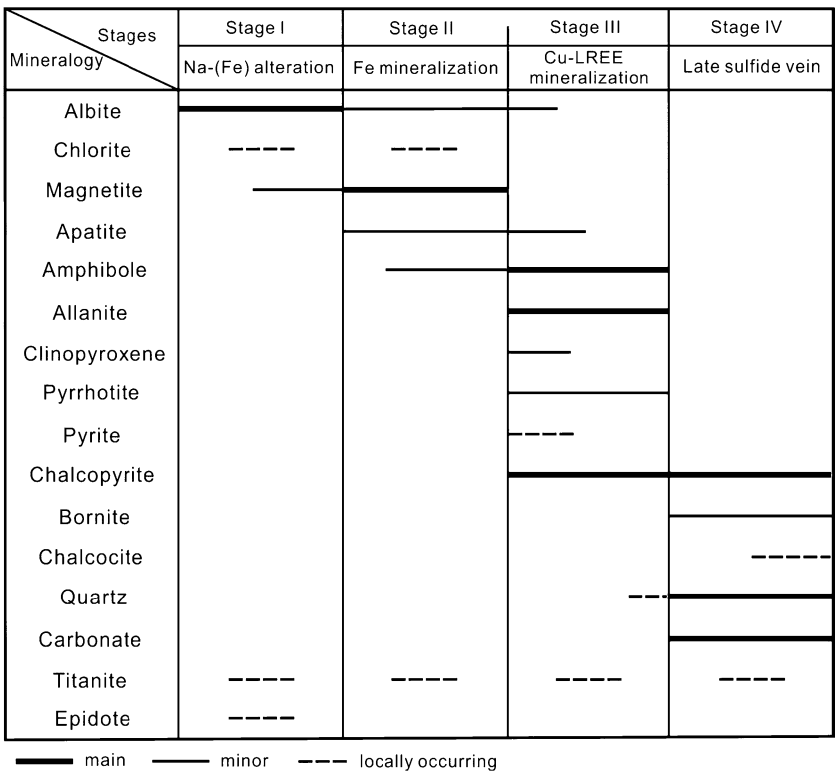

Fig. 4 Paragenetic sequence of alteration and mineralization in the Longbohe deposit

in which both minerals are closely associated with albite and magnetite.

Stage II: Fe mineralization

This stage is characterized by abundant magnetite and apatite that are closely associated with Ca-Na alteration forming amphibole and albite, and subordinate but variable proportions of clinopyroxene, chlorite and titanite (Fig. 5b, c, d). Both magnetite and apatite are euhedral to subhedral in shapes and homogeneous under high-resolution BSE images (Fig. 5f) Amphibole crystals are of actinolite composition, while albite is characterized by high Na/(Na + Ca + K) ratios (0.99 to 1.00), similar to those of Stage I. Clinopyroxene crystals are of hedenbergite composition, and chlorite has ripidolite to brunsvigite composition.

Stage III: Cu-LREE mineralization

This stage is dominated by chalcopyrite and LREE-rich allanite with subordinate pyrrhotite and pyrite. It is associated with Ca alteration forming variable amounts of amphibole, titanite, apatite, and albite (Fig. 6a, b). Chalcopyrite crystals are angular in shapes and are closely associated with amphibole. Pyrrhotite is also generally angular in shapes, and is intergrown with chalcopyrite, pyrite, amphibole, and albite (Fig. 6c, d). It is common in the mixed oxide-sulfide ores that the assemblages of this stage overprint earlier magnetite of Stage II (Fig. 6a).

Amphibole crystals have ferropargasite to ferrodenite composition with elevated K_2O contents (1.60 to 1.88 wt%) relative to those in Stage II. Albite grains have elevated CaO and K_2O contents relative to those of Stages I and II, with much lower Na/(Na + Ca + K) ratios (0.77 to 0.80).

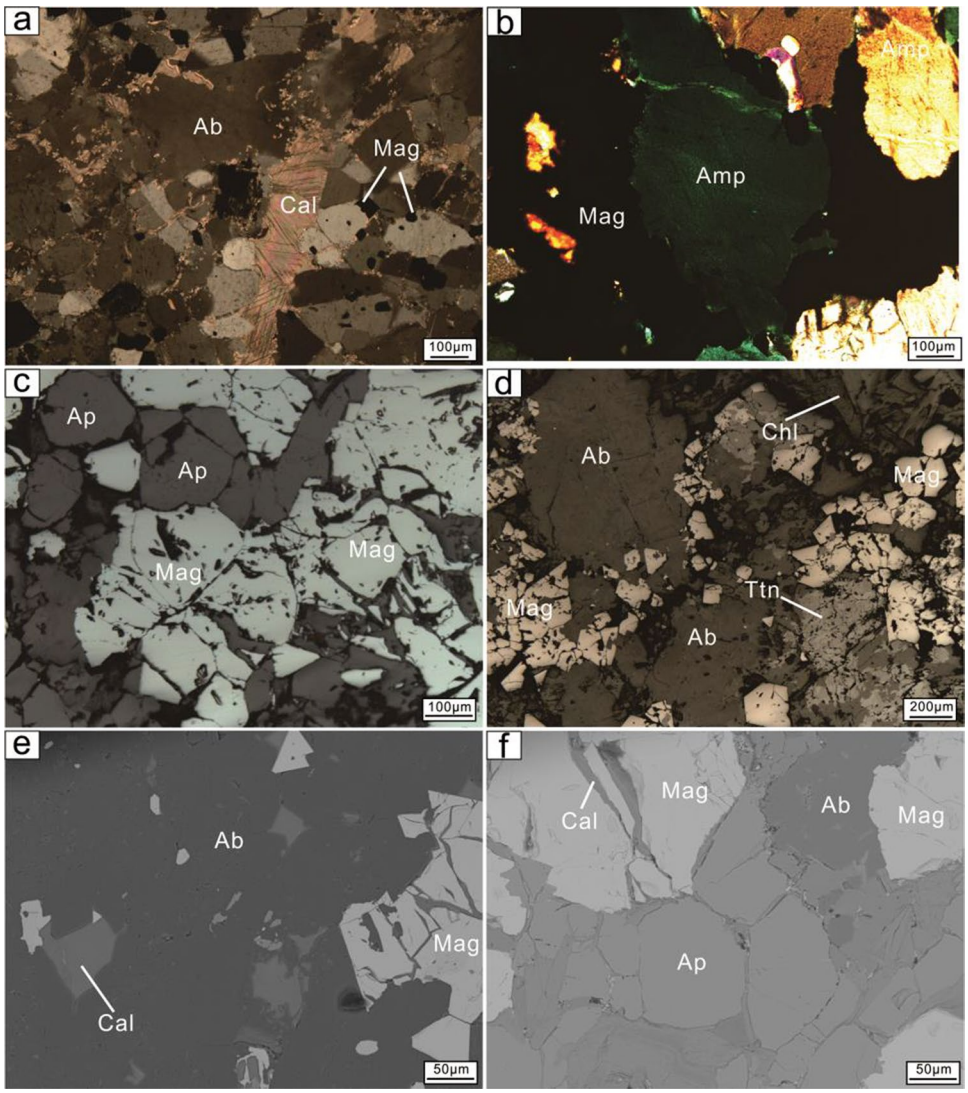

Fig. 5 Photomicrographs of altered rocks and Fe ores. **a** Albitized rock is mainly composed of albite grains and minor magnetite. Note cross-cutting late calcite vein. **b** Disseminated Fe ore is composed of magnetite and amphibole (actinolite). **c** Massive Fe ore is composed of intergrown magnetite and apatite. **d** Disseminated Fe ore showing that both titanite and chlorite, associated with magnetite, are locally present. **e** BSE image of albitized rock. Note that both albite and magnetite are homogeneous. **f** BSE image of massive Fe ore. Note that both apatite and magnetite are closely associated, and exhibit homogeneous texture. Amp: amphibole, Chl: chlorite, Ttn: titanite. Other abbreviations as in Fig. 3

Stage IV: post-deformation veins

Mineral assemblages of Stages I, II and III are variably foliated or deformed, and are crosscut by Stage IV veins that are not deformed or foliated (Fig. 3d). These veins are mineralized and are composed of variable amounts of chalcopyrite, bornite, chalcocite, quartz and carbonate minerals (Fig. 6e, f). Chalcopyrite is relatively earlier, as it is replaced by bornite and chalcocite (Fig. 6e). Bornite is slightly earlier than chalcocite, as it is locally replaced by chalcocite (Fig. 6e). Carbonate minerals are mainly calcite and dolomite (Fig. 6f).

Analytical methods

Electron microprobe analysis

The major element compositions of minerals were measured using a JEOL JXA-8530F microprobe at the State Key Laboratory of Ore Deposit Geochemistry, Institute of Geochemistry, Chinese Academy of Sciences, Guiyang, China. A 25-kV accelerating voltage and a 10-nA beam current were used in the analyses. The beam spot size was set at 10 μm. For analysis of amphibole, the standard samples were tugtupite for Cl, apatite for F, chlorite for Cr, kaersutite for Ca, Ti, Na, Si, Al, Mg, K, Mn and Fe. For clinopyroxene, the

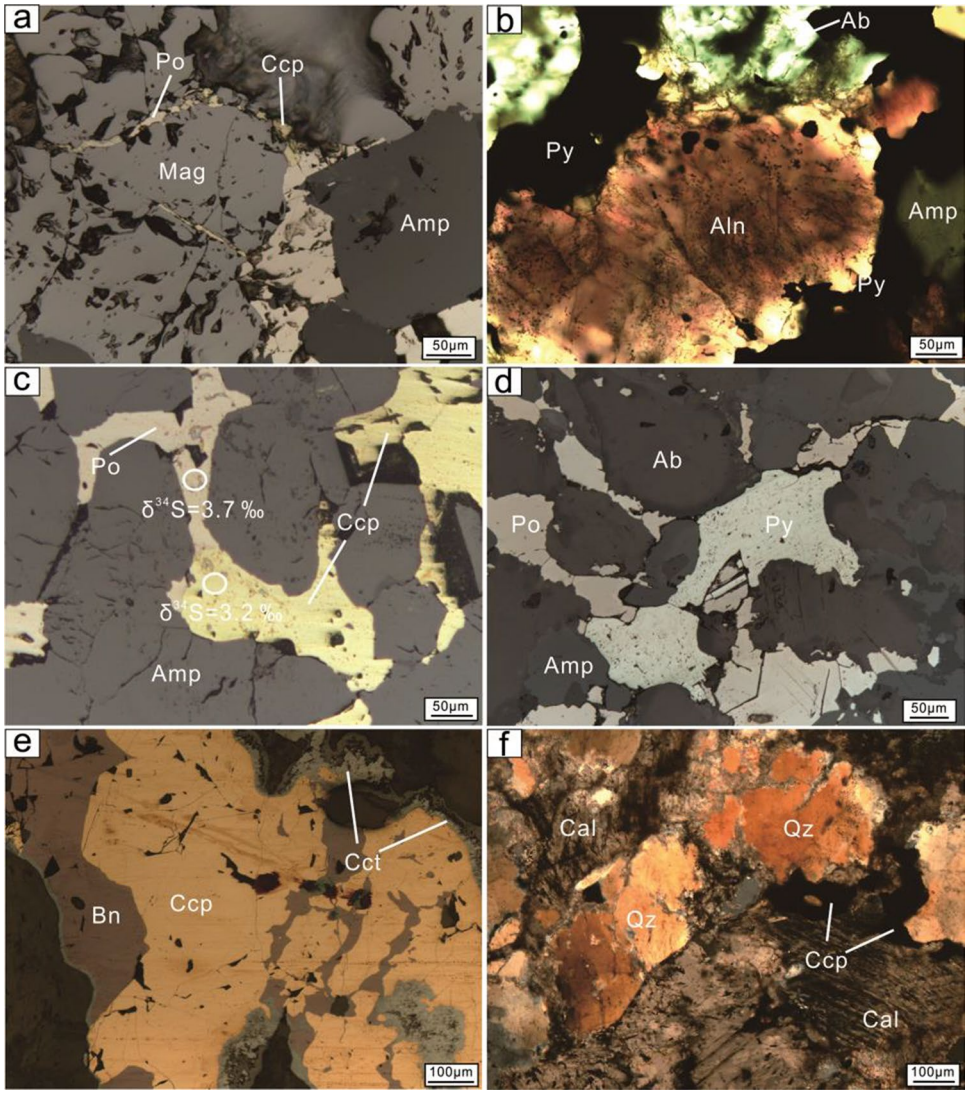

Fig. 6 Photomicrographs of different Fe-Cu or Cu ores. **a** Fe-Cu ore showing that early magnetite is crosscut by Cu-sulfides. **b** Cu ore composed of intergrown allanite, pyrite, amphibole and albite. **c** Cu ore. Note that pyrrhotite is intergrown with chalcopyrite and amphibole with regular contacts. Also shown are the locations for S isotopic values. **d** Cu ore. Note that pyrrhotite is intergrown with pyrite, albite, and amphibole. **e** Late sulfide vein showing that chalcopyrite is replaced by bornite and chalcocite. **f** Late sulfide vein consisting mainly of quartz and calcite with minor chalcopyrite. Aln: allanite, Bn: bornite, Py: pyrite. Other abbreviations as in Figs. 3 and 5

standard samples were tugtupite for Cl, apatite for F, chlorite for Cr, plagioclase for Si, kaersutite for Ca, Ti, Na, Al, Mg, K, Mn and Fe. For analysis of albite, the standard samples were tugtupite for Cl, apatite for F, chlorite for Cr, albite for Na, Si and Al, plagioclase for Ca and Mg, orthoclase for K and Fe, kaersutite for Ti and Mn. For analysis of chlorite, the standard samples were tugtupite for Cl, apatite for F, chlorite for Cr, Si, Al, Mg and Ni, kaersutite for Ca, Ti, Na, K, Mn and Fe. Under these conditions, the analytical errors are generally estimated to be < 1% at the > 10 wt% level, < 5% at the 1 to 10 wt% level, and > 5% at the < 1 wt% level.

Trace elements analyses of magnetite

In situ trace elements analyses of magnetite were conducted by an *Analyte Excite* 193-nm laser-ablation system coupled with an Agilent 7700 × quadrupole ICP-MS at Nanjing FocuMS analytical laboratory. A laser spot size of 40 μm and a repetition rate of 6 Hz for 40 s of data acquisition with an energy density of 12 J/cm^2 were utilized during the analysis. Helium was applied as carrier gas. Element contents were calibrated against multiple reference materials (BIR-1G, BHVO-2G, BCR-2G and GSE-1G) without applying internal standards (Liu et al. 2008). Off-line data reduction was carried out using ICPMSDataCal (Liu et al. 2008).

Bulk sample analysis

Major elements were determined by X-ray fluorescence spectrometry (P61-XRF26s method), and trace elements were analyzed by inductively coupled plasma mass spectrometry (M61-MS81 method) at the Mineral Division of ALS Laboratory Group, Guangzhou. The analytical precision was usually 1 to 3% for elements at > 1 wt%, and about 10% relative for elements present in concentrations < 1 wt%. For trace elements, the analytical precision was generally better than 5% based on replicate analyses of standard samples.

Zircon cathodoluminescence (CL), U–Pb dating and trace elements analysis

Zircon grains were selected from crushed samples using standard gravity and magnetic techniques. The separated grains were mounted in epoxy resin. Zircon grains were examined in transmitted, reflected and CL light to reveal their internal textures before U–Pb analysis. Cathodoluminescence (CL) analysis was carried out on polished sections using a Gatan MONO CL3 detector at the Guangzhou Institute of Geochemistry, Chinese Academy of Sciences, Guangzhou, China. The zircon U–Pb and trace elements analyses was conducted using a GeoLas Pro 193 nm ArF excimer laser ablation system equipped with an Agilent 7700 × inductively coupled plasma mass spectrometer (ICP-MS), at the State Key Laboratory of Ore Deposit Geochemistry, Institute of Geochemistry, Chinese Academy of Sciences, Guiyang, China. Each analysis incorporated a background acquisition of approximately 20 s followed by 40 s of data acquisition, with a 5 Hz repetition rate on a stationary spot of 33 μm. Helium mixed with argon was applied as carrier gas. Zircon 91500 and NIST 610 were utilized as the external standards for U–Pb dating and trace elements, respectively. Data reduction was carried out using ICPMSDataCal (Liu et al. 2008, 2010) and then processed using the ISOPLOT program (Ludwig 2003).

Zircon Hf isotope analysis

Different types of zircon grains were selected for Lu–Hf isotope analyses after U–Pb dating. Zircon Lu–Hf isotope analyses were carried out using a RESOlution-S155 laser-ablation system coupled with *Nu Plasma III* MC-ICP-MS at the State Key Laboratory of Ore Deposit Geochemistry, Institute of Geochemistry, Chinese Academy of Sciences, Guiyang, China. A laser spot size of 60 μm and a repetition rate of 6 Hz for 40 s of data acquisition with an energy density of 6.0 J/cm^2 were used during the analysis. Zircon 91500, Plešovice, Mud Tank and Penglai were used as reference standards. Every five analyses were followed by one analysis of Penglai to correct time-dependent drift of sensitivity and mass discrimination. Correction for isobaric interference of ^{176}Lu on ^{176}Hf and ^{176}Yb on ^{176}Hf was corrected by using the recommended ^{176}Lu/^{175}Lu ratio of 0.02655 (Machado and Simonetti 2001) and ^{176}Yb/^{172}Yb ratio of 0.5887 (Vervoort et al. 2004) to calculate ^{176}Lu/^{177}Hf and ^{176}Yb/^{177}Hf, respectively.

In situ *S* isotope analysis

Sulfide minerals of different stages were chosen for in situ sulfur isotope analysis. The analysis was performed in thin section, using the Nu Plasma 1700 MC-ICP-MS together with the RESOlution M-50 laser ablation system equipped with a 193 nm ArF CompexPro102 excimer laser at the State

Key Laboratory of Continental Dynamics, Northwest University, Xi'an, China. The main analytical procedure was described by Bao et al. (2017) and Yuan et al. (2018). Instrument drift and mass bias were corrected using a standard-sample bracketing method with repeated measurements of the standard, before and after each sample. Helium gas was employed as carrier gas (gas flows = 0.28 L/min) and Ar gas was used as makeup gas (gas flows = 0.6 L/min). Each spot was ablated at a spatial resolution of 30 μm at 4 Hz, using a fluency 3 J/cm^2, and comprises approximately 30 s background acquisition and 50 s sample data acquisition. All measured $^{34}S/^{32}S$ ratios were normalized to Vienna Canyon Diablo Troilite compositions (V-CDT). Two in-house sulfur reference materials of pyrite (PY-4, $\delta^{34}S = 1.7 \pm 0.3$ ‰; Bao et al. 2017) and chalcopyrite (CPY-1, $\delta^{34}S = 4.2 \pm 0.3$ ‰; Bao et al. 2017) were used as external standard. A pressed sulfide powder tablet of sphalerite (PSPT-3, $\delta^{34}S = 26.4 \pm 0.2$ ‰; Bao et al. 2017) was used for quality control.

Oxygen isotope analysis

Magnetite, albite and apatite were concentrated by magnetic and density separation techniques, respectively. These minerals were handpicked under the binocular microscope. The purity of separates is estimated to be 95%. Oxygen isotope analyses of magnetite, albite and apatite were performed at the Analytical Laboratory of the Beijing Research Institute of Uranium Geology, Beijing, China. Oxygen was liberated by reacting samples with BrF_5, and then oxygen was reacted with carbon rods to produce CO_2. The extracted CO_2 for O isotope analysis was measured using a MAT253 mass spectrometer. The results are expressed relative to the Vienna PeeDee Belemnite (V-PDB) standard, but the $\delta^{18}O$ values were listed are referenced to the Vienna Standard Mean Water (V-SMOW). The $\delta^{18}O_{V\text{-}PDB}$ was converted to $\delta^{18}O_{V\text{-}SMOW}$ by using Coplen et al. (1983): $\delta^{18}O_{V\text{-}SMOW} = 1.03091\delta^{18}O_{V\text{-}PDB} + 30.91$. The analytical uncertainty is ± 0.2 ‰.

Quartz grains from late sulfide veins (Stage IV) were handpicked under the binocular microscope. The purity of quartz separates is estimated to be > 95%. Oxygen isotopes of quartz were measured at the State Key Laboratory of Ore Deposit Geochemistry, Institute of Geochemistry, Chinese Academy of Sciences, Guiyang, China. The oxygen was liberated from the reaction of quartz with BrF_5 (Clayton and Mayeda 1963) and then converted to CO_2 on a platinum-coated carbon rod. The $\delta^{18}O$ determinations were done using a MAT-253 mass spectrometer. Values of $\delta^{18}O$ are reported in units of per mil (‰) relative to Vienna Standard Mean Water (V-SMOW). The analytical uncertainty is ± 0.2 ‰.

Carbon and oxygen isotope analysis of calcite

Calcite separates from late sulfide veins (Stage IV) were handpicking under the binocular microscope to achieve purity > 95%. Calcite C and O isotopes were measured at the State Key Laboratory of Ore Deposit Geochemistry, Institute of Geochemistry, Chinese Academy of Sciences, Guiyang, China. The powered calcite was reacted with concentrated phosphoric acid in sealed vessels, and then CO_2 released was measured for C and O isotopic analyses. Values of $\delta^{13}C$ and $\delta^{18}O$ are reported relative to the Vienna PeeDee Belemnite (V-PDB) standard. However, the $\delta^{18}O$ values are listed relative to Vienna Standard Mean Water (V-SMOW). The V-PDB and V-SMOW relationship is: $\delta^{18}O_{V\text{-}SMOW} = 1.03091\delta^{18}O_{V\text{-}PDB} + 30.91$ (Coplen et al. 1983). The $\delta^{13}C$ and $\delta^{18}O$ values are reported in units of per mil (‰) and the analytical precision is generally ± 0.05 ‰ for $\delta^{13}C$ and ± 0.2 ‰ for $\delta^{18}O$.

Magnetite and bulk ore/rock geochemistry

The analytical results are provided in ESM Tables 2 and 4.

Trace elements of magnetite

Trace elements in magnetite of Stage II contain relatively high Mg (5.3–217 ppm), Al (225–2988 ppm), Si (139–3093 ppm), Ti (29.2–3717 ppm), Mn (43.5–619 ppm), and V (14.3–818 ppm); other elements such as Na, P, Ga,

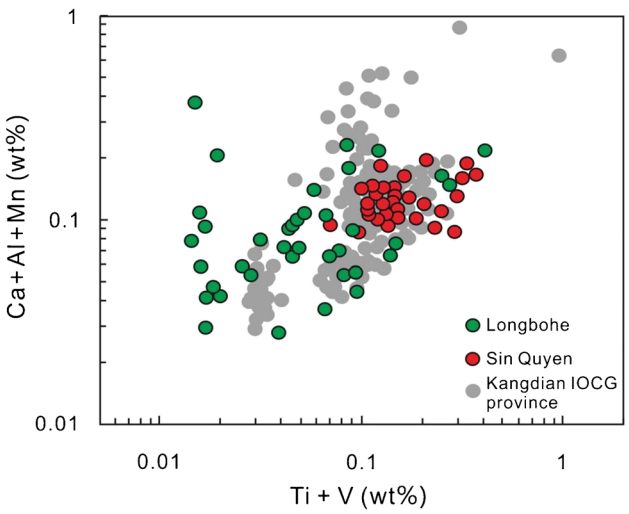

Fig. 7 Plots of Ca + Al + Mn vs. Ti + V of magnetite from the Longbohe and Sin Quyen deposits. Also shown are the magnetite data of the Lala, Dahongshan and Yinachang deposits in the Kangdian IOCG province (Chen et al. 2015)

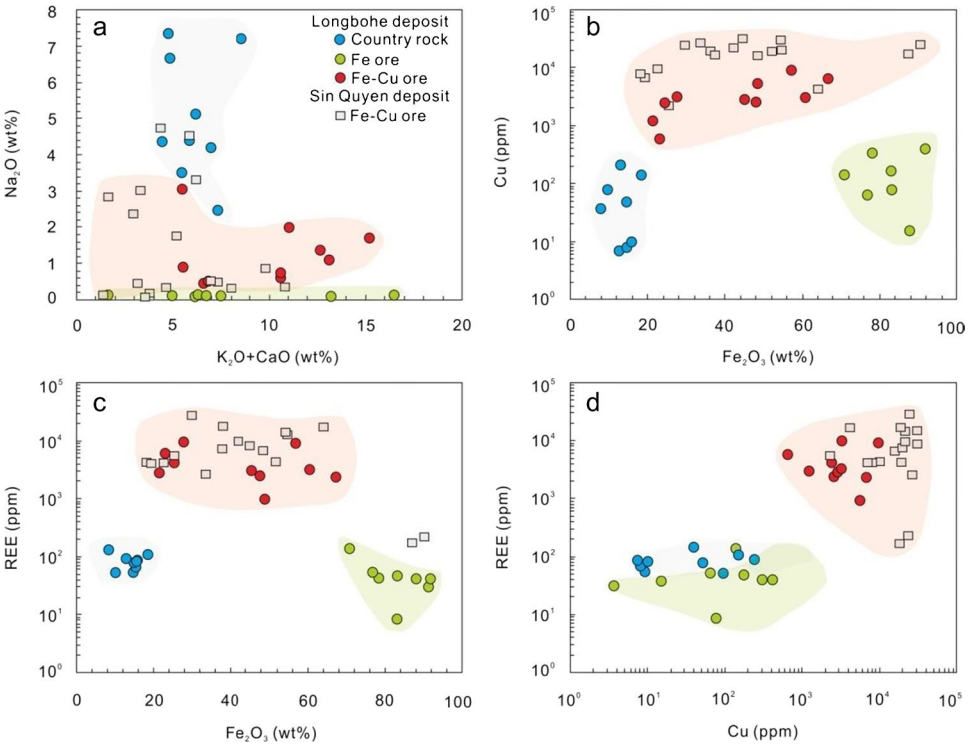

Fig. 8 Plots of Na_2O vs. K_2O+CaO (a), Cu vs. $Fe_2O_{3(total)}$ (b), REE vs. $Fe_2O_{3(total)}$ (c), and REE vs. Cu (d) for bulk samples from the Longbohe and Sin Quyen deposits. The data of the Sin Quyen deposit are from Li and Zhou (2018)

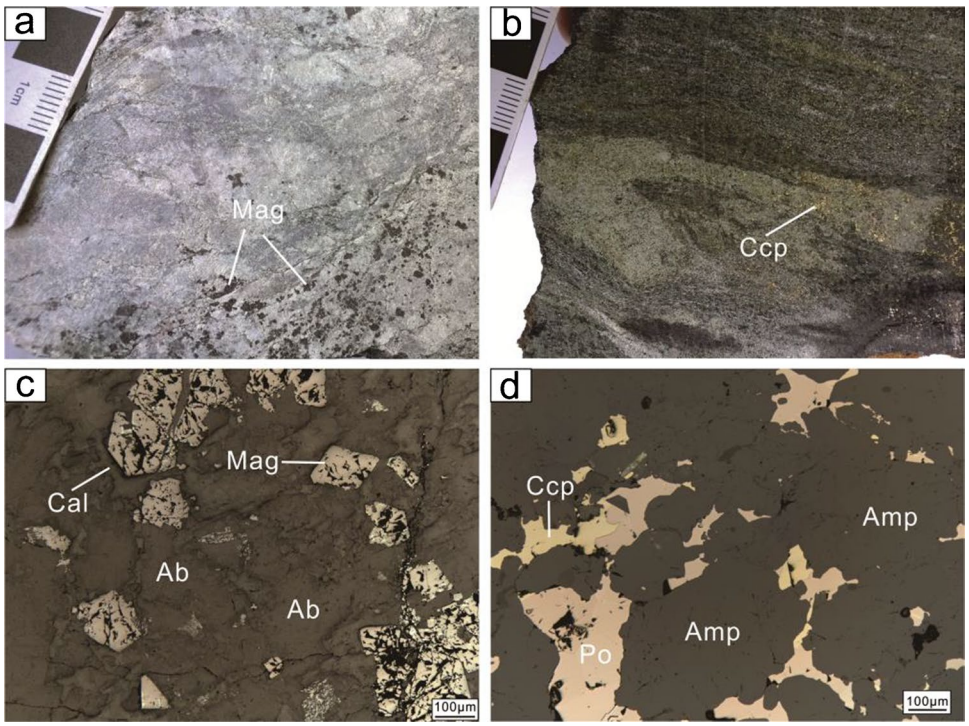

Fig. 9 The Fe and Cu ore samples for zircon analysis. **a** Fe ore (sample LBH17-66). Note that it is composed of albite and disseminated magnetite. **b** Cu ore (sample LBH17-20). Note that it was strongly deformed and consists of chalcopyrite and amphibole. **c** Micro-feature of sample LBH17-66 showing that it consists mainly of magnetite and albite. **d** Micro-feature of sample LBH17-20 showing that it consists mainly of chalcopyrite, pyrrhotite, and amphibole. Mineral abbreviations as in Figs. 3 and 5

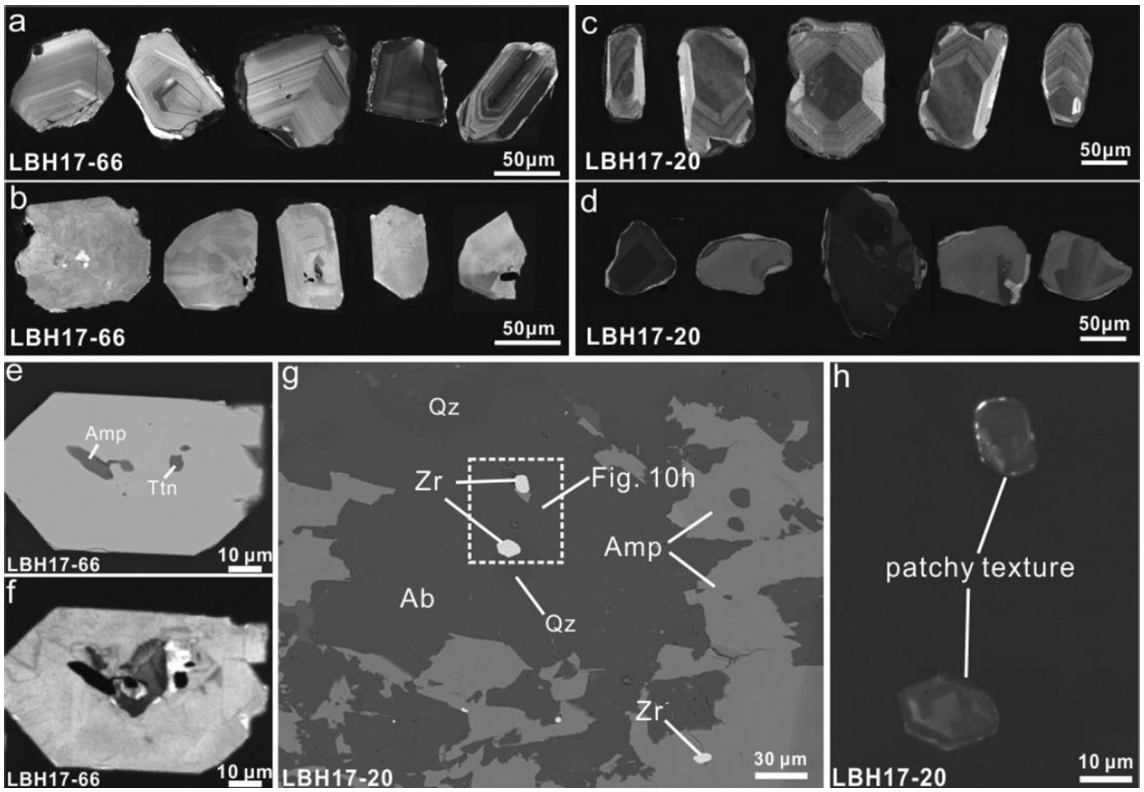

Fig. 10 Photomicrographs of zircon from samples LBH17-66 and LBH17-20. **a** and **b** CL images of Type 1 and Type 2 zircon in sample LBH17-66, respectively. **c** and **d** CL images of Type 1 and Type 2 zircon in sample LBH17-20, respectively. **e** and **f** BSE and CL images of Type 2 zircon from Fe ore. Note that Type 2 zircon contains mineral inclusions of hydrothermal amphibole and titanite. **g** and **h** BSE and CL images of Type 2 zircon in thin section of sample LBH17-20. Note that Type 2 zircon has close association with albite, quartz, and amphibole. Zr: zircon. Other abbreviations as in Figs. 3 and 5

Co, Ni, Cr, Zn and Ge are relatively minor, with concentrations ranging from several ppm to < 1 ppm. We have also analyzed the trace elemental compositions of magnetite from the Sin Quyen deposit. The results show that the magnetite compositions for both deposits are undistinguishable in the Ca + Al + Mn versus Ti + V diagram (Fig. 7).

Bulk sample compositions

The detailed information for selected samples is available in ESM Table 3. Twenty-seven samples are selected for major and trace elements analyses, including albitized host rocks, Fe and Fe-Cu ores. These samples display large chemical variations that are well correlated with relative amounts of minerals in these rocks/ores. For example, the Na-(Fe) altered rocks have highest Na_2O (up to 7.41 wt%), whereas the Fe and Fe-Cu ores have the highest Fe (Total Fe_2O_3 up to 91.52 wt%), Cu (> 10,000 ppm), and $K_2O + CaO$ (up to 16.40 wt%) (Fig. 8a). In addition, REE, P_2O_5 and TiO_2 contents range from 8.00 to 10,063 ppm, 0.09 to 8.83 wt% and from 0.01 to 2.15 wt%, respectively, corresponding to the variable amounts of allanite, apatite and titanite (Fig. 8b, c, d). It is notable that massive Fe ores have highest contents of P_2O_5 and Fe_2O_3, consistent with the close association of magnetite and apatite.

Zircon trace elemental, U–Pb and Lu–Hf isotopic compositions

Two ore samples, LBH17-66 and LBH17-20, were selected for the trace elemental, U–Pb and Lu–Hf isotopic analyses of zircon (Fig. 2a). The first sample is essentially a magnetite-mineralized meta-volcanic rock with zircon U–Pb age of ~ 1700 Ma (Liu and Chen 2019), which consists mainly of albite, magnetite, and chlorite (Fig. 9a, c). Minor calcite veinlets are also present in this sample, crosscutting the ore minerals mentioned above (Fig. 9c). The latter is a

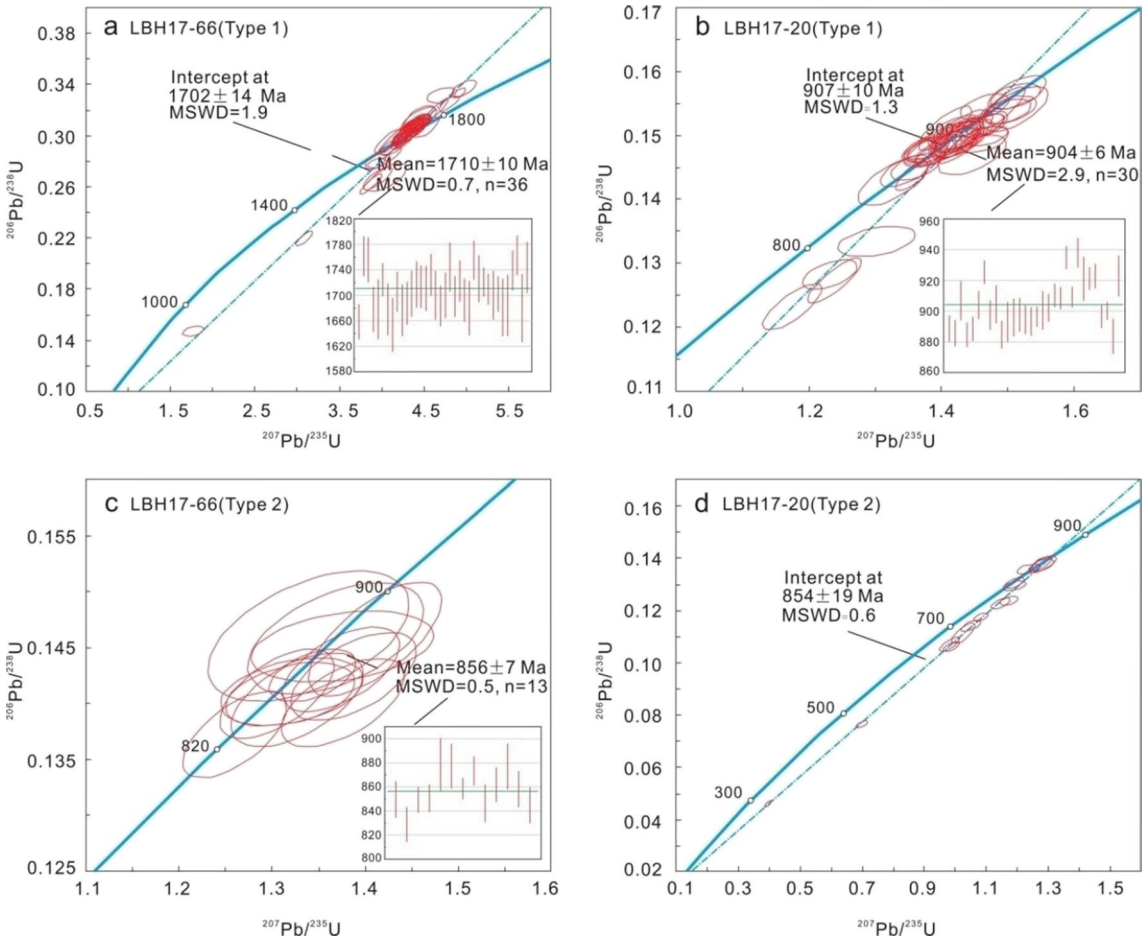

Fig. 11 Zircon U–Pb concordia plots for Type 1 zircons from LBH17-66 (**a**) and LBH17-20 (**b**), and Type 2 zircons from LBH17-66 (**c**) and LBH17-20 (**d**)

Cu-mineralized meta-sedimentary rock with ages as young as ~ 900 Ma (Liu and Chen 2019). This sample is composed mainly of chalcopyrite, pyrrhotite, amphibole, allanite, and albite (Fig. 9b, d). The whole datasets are provided in ESM Tables 5, 6 and 7.

Sample LBH17-66

Two types of zircon grains have been identified in sample LBH17-66. Type 1 zircon grains have distinct oscillatory zoning in CL images and high Th/U ratios (> 0.4; Figs. 10a, 12a). Excluding several analyses that have obviously old or discrete U–Pb ages, the remaining analyses for Type 1 zircon yield an upper intercept age of 1702 ± 14 Ma (MSWD = 1.9) and a weighted mean $^{207}Pb/^{206}Pb$ age of 1710 ± 10 Ma (MSWD = 0.7; Fig. 11a). The $^{176}Lu/^{177}Hf$ and $^{176}Hf/^{177}Hf$ ratios range from 0.000910 to 0.003949 and 0.281661 to 0.281943, respectively.

In contrast, Type 2 zircon grains exhibit distinctly homogeneous features in CL images (Fig. 10b), and commonly contain inclusions of hydrothermal minerals such as amphibole and titanite (Fig. 10e, f). Compared to Type 1 zircon, they have relatively low Th/U ratios (0.15 to 0.56), as well as lower contents of Ti and Y and relatively weak Eu anomalies (Fig. 12a, b, c). Most analyses of these grains are concordant in the concordia diagram, and yield a much younger weighted mean $^{206}Pb/^{208}U$ age of 856 ± 7 Ma (MSWD = 0.5; Fig. 11c). They have also different $^{176}Lu/^{177}Hf$ (0.000373 to 0.001083) and $^{176}Hf/^{177}Hf$ (0.282468 to 0.282607) ratios, corresponding to distinctly depleted, initial $^{176}Hf/^{177}Hf$ ratios and $\varepsilon_{Hf(t)}$ values at ~ 850 Ma ranging from 0.282451 to 0.282595 and 7.5 to 12.7, respectively (Fig. 13b). Such values are remarkably higher than those of Type 1 zircon grains which have calculated $^{176}Hf/^{177}Hf$ and $\varepsilon_{Hf(t)}$ values ranging from 0.281646 to

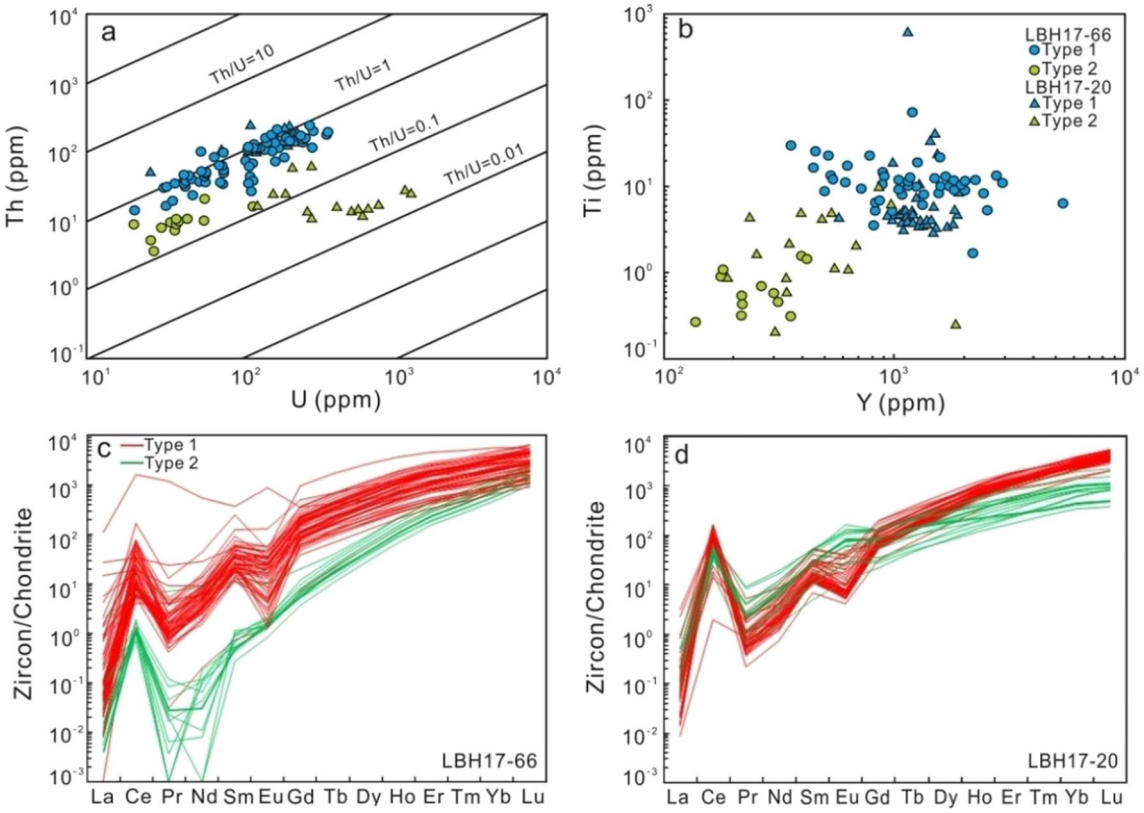

Fig. 12 Plots of Th vs. U (**a**), Ti vs. Y (**b**), and chondrite-normalized REE patterns (**c** and **d**) for Type 1 and 2 zircons from sample LBH17-66 and LBH17-20. The chondrite data are from McDonough and Sun (1995)

0.281907 and -21.0 to -12.1 at ~ 850 Ma, respectively (Fig. 13a).

Sample LBH17-20

In sample LBH17-20, two types of zircon grains were recognized as well. Type 1 zircon grains have distinct oscillatory zoning in CL images (Fig. 10c), and exhibit high Th/U ratios (> 0.5; Fig. 12a). Most analyses are concordant, and have $^{207}Pb/^{206}Pb$ or $^{206}Pb/^{208}U$ ages ranging from ~ 860 to ~ 1800 Ma with a cluster around 900 Ma (ESM Table 6). This cluster of analyses yields an upper intercept age of 907 ± 10 Ma (MSWD = 1.3) and a weighted mean $^{206}Pb/^{208}U$ age of 904 ± 6 Ma (MSWD = 2.9; Fig. 11b). These grains have $^{176}Lu/^{177}Hf$ and $^{176}Hf/^{177}Hf$ ratios ranging from 0.000968 to 0.002025 and 0.282392 to 0.282567, respectively.

Type 2 zircon grains are characterized by homogeneous or patchy textures in CL images (Fig. 10d), and are closely associated with hydrothermal minerals of albite, amphibole, and quartz (Fig. 10g, h). Compared to Type 1 zircon, they have remarkably low Th/U ratios (0.02 to 0.21), low contents of Ti and Y, and distinctly positive Eu anomalies (Fig. 12a, b, d). All analyses of Type 2 zircon form a discordant trend line with an upper intercept age of 854 ± 19 Ma (MSWD = 0.6; Fig. 11d), similar to Type 2 zircon in sample LBH17-66. They have initial $^{176}Hf/^{177}Hf$ ratios and $\varepsilon_{Hf(t)}$ values (calculated for ~ 850 Ma) varying from 0.282245 to 0.282351 and 0.3 to 4.0, respectively, lower than those of Type 1 zircon grains in this sample, which have initial $^{176}Hf/^{177}Hf$ and $\varepsilon_{Hf(t)}$ values (calculated for ~ 850 Ma) ranging from 0.282396 to 0.282546 and 4.7 to 10.9, respectively (Fig. 13a, b).

Stable isotope geochemistry

The analytical results of S, O, and C isotopes for sulfide, oxide, phosphate, and silicate minerals are provided in ESM Tables 8 and 9.

In-situ sulfur isotopic compositions

In-situ sulfur isotopic compositions of sulfides from Stage III have $\delta^{34}S_{V\text{-}CDT}$ values ranging from 1.2 to 3.7 ‰

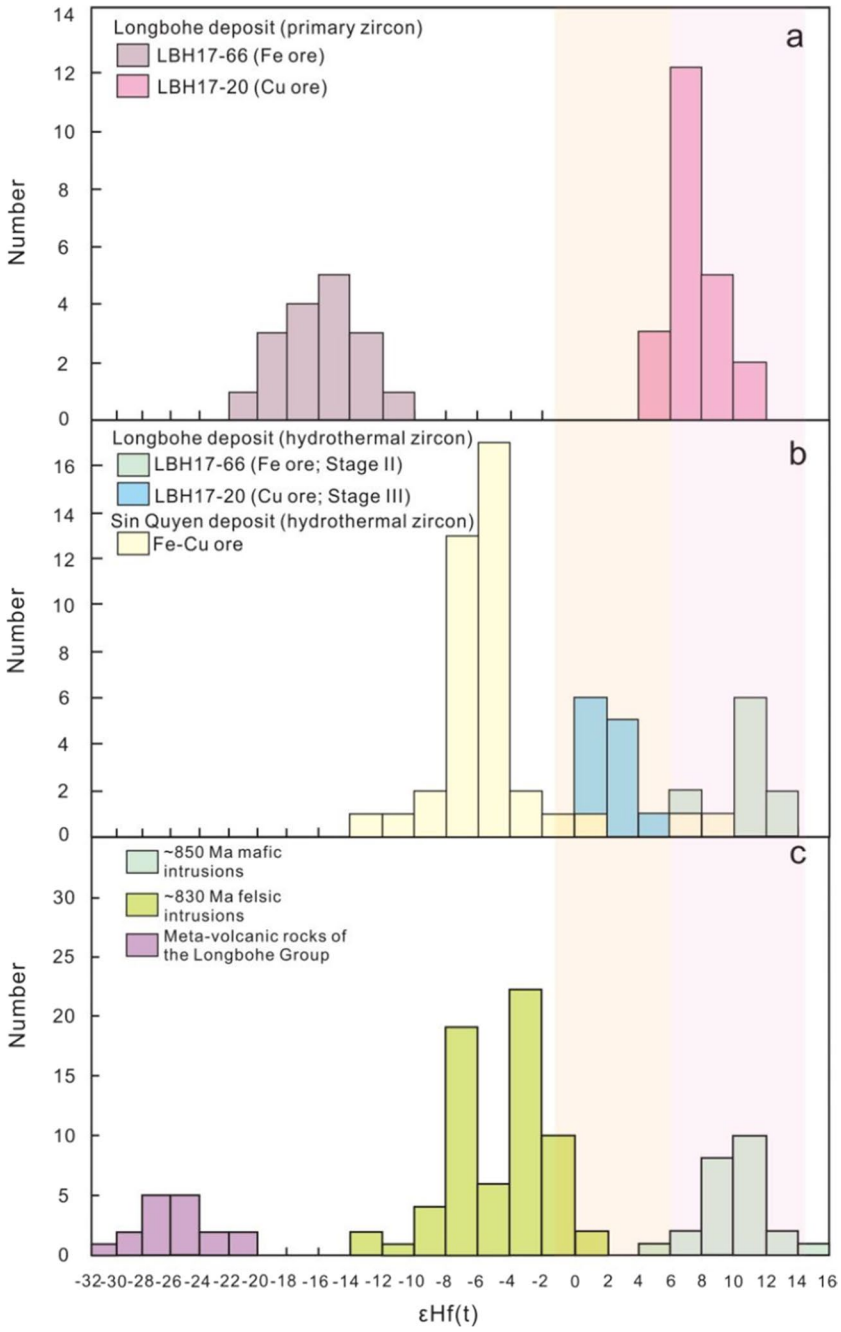

Fig. 13 Histograms showing $\varepsilon_{Hf(t)}$ values of zircon and whole rocks. **a** $\varepsilon_{Hf(t)}$ values of primary magmatic zircon (Type 1) from LBH17-66 and LBH17-20 in the Longbohe deposit. **b** $\varepsilon_{Hf(t)}$ values of hydrothermal zircon (Type 2) from LBH17-66 and LBH17-20 in the Longbohe deposit. Also shown are the data of the Sin Quyen deposit (Li and Zhou 2018). **c** $\varepsilon_{Hf(t)}$ values of magmatic zircon from ~ 850 Ma mafic intrusions in the western Yangtze Block, ~ 830 Ma felsic intrusions in the ASRR shear zone, and meta-volcanic rocks of the Longbohe Group. Note that the data for the mafic and felsic intrusions are from Meng et al. (2015), Li et al. (2018b) and Chen et al. (2019), while those of the meta-volcanic rocks are from our unpublished dataset (calculated at 850 Ma)

(Fig. 14a), while those of Stage IV range from 0.6 to 7.7 ‰ (Fig. 14b). As fluid inclusion data for Stage III are not available, the sulfur isotopic geothermometer of coexisting mineral pairs was used to estimate the temperatures of this stage (Fig. 6c). In order to reduce the potential overprint of regional metamorphism, only chalcopyrite-pyrrhotite pairs from relatively poorly deformed samples (e.g., LBH17-11, LBH17-21, and LBH17-25) were selected for temperature calculation. It is notable that the selected pairs may have reached isotopic equilibrium on the basis that the *in-situ* $\delta^{34}S_{V\text{-}CDT}$ values of pyrrhotite are reasonably heavier than those of chalcopyrite (Zheng and Chen 2000). Using the $\delta^{34}S_{V\text{-}CDT}$ values of the chalcopyrite-pyrrhotite pairs and related fractionation factor (Zheng and Chen 2000), the calculated temperatures for Stage III range from 332 to 402 ºC. Temperatures in Stage IV are available from

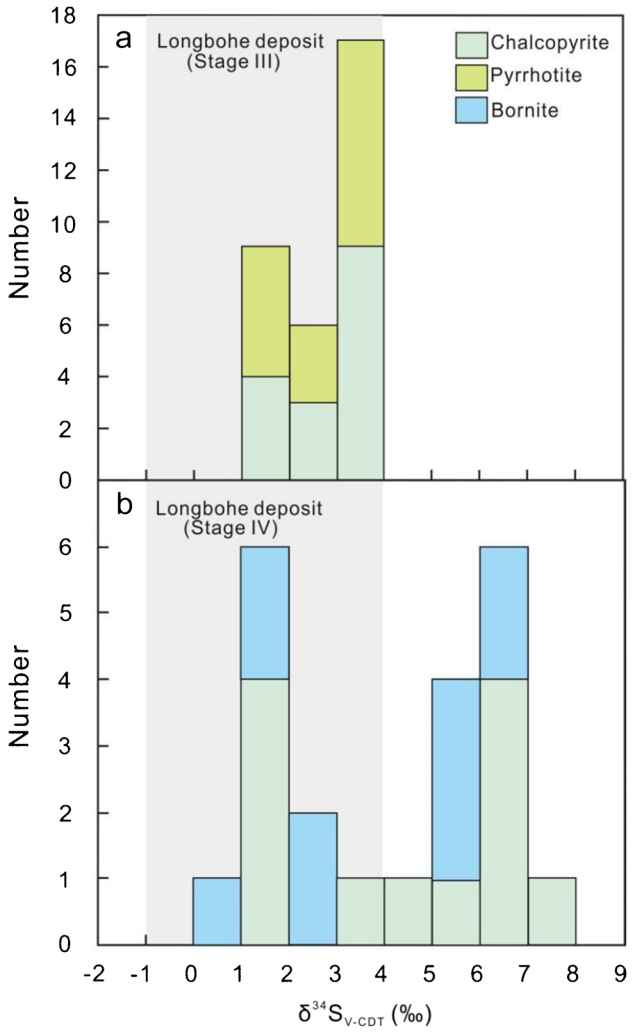

Fig. 14 Sulfur isotopic compositions of sulfides in Stages III (**a**) and IV (**b**) from the Longbohe deposit. Data of the Sin Quyen deposit in grey (Li et al. 2018a; Li and Zhou 2018)

fluid inclusion data (Cui 2007). The $\delta^{34}S_{V\text{-}CDT}$ values of sulfides in Stage IV show two peaks at ~ 1.5 ‰ and ~ 6.0 ‰ (Fig. 14b). Considering that sulfide minerals are the dominant phases in Stages III and IV without hematite or sulfate (e.g., indicating low f_{O2} conditions), it is suggested that the sulfur species dissolved in the fluids were assumed to be mainly H_2S. As such, the $\delta^{34}S_{V\text{-}CDT}$ values of sulfides could be used to represent those of the parental fluids (Ohmoto 1972; Ohmoto and Rye 1979).

Oxygen isotopic compositions

As fluid inclusions are poorly developed in the samples, the oxygen isotopic analyses of mineral pairs in some stages were tentatively conducted, in order to calculate the temperatures. Even so, the calculation for Stage I cannot be achieved due to lack of suitable pairs in the samples of this stage. Instead, coexisting apatite and magnetite pairs are common in the massive Fe ores of Stage II (Fig. 5c, f), thus were good candidates for O isotopic analyses. At the very beginning, these candidate samples were carefully checked in high-resolution BSE imaging to avoid potentially extensive modification. Our results show that both minerals (i.e., the pairs) in Stage II are homogeneous and commonly closely associated, with regular contacts (Fig. 5f). These features indicate that the selected magnetite-apatite pairs should be isotopically equilibrated, and thus their O isotopic ratios could be used for temperature calculation.

Our new results show that albite and magnetite crystals in Stage I have $\delta^{18}O_{V\text{-}SMOW}$ values ranging from 9.5 to 10.5 ‰ and -1.7 to 0.1 ‰, respectively, while those of coexisting magnetite and apatite in Stage II range from 3.7 to 5.6 ‰ and 10.4 to 11.0 ‰, respectively. The calculated temperatures for apatite-magnetite pairs in Stage II range from 515 to 670 ºC, corresponding to the calculated $\delta^{18}O$ values ranging from 10.8 to 11.7 ‰. For Stage I, no mineral pairs are available for calculation, but its comparable mineral assemblages and locally transitional contacts with Stage II ores allow us to propose that the temperature for Stage I should be broadly comparable to that of Stage II. Therefore, using the maximum value of ~ 670 ºC, the calculated $\delta^{18}O$ values of Stage I fluids were estimated to be ranging from 4.3 to 10.1 ‰.

Quartz and calcite crystals in Stage IV have $\delta^{18}O_{V\text{-}SMOW}$ values varying from 10.4 to 12.1 ‰ and 10.1 to 11.3 ‰, respectively. Using the temperature of ~ 220 ºC (estimated by previous thermometry data of fluid inclusions; Cui 2007), the $\delta^{18}O$ values of the fluids were calculated to be ranging from -0.2 to 3.2 ‰.

Carbon isotopic compositions of calcite

Calcite in Stage IV has $\delta^{13}C_{V\text{-}PDB}$ values from -2.4 to -1.5 ‰. Using the temperatures of ~ 220 ºC (Cui 2007), the $\delta^{13}C$ values of the fluids were calculated to range from -3.2 to -2.3 ‰ (Fig. 15b).

Discussion

Sources and evolution of ore-forming fluids

In this study, we estimated the temperatures for different stages by using isotopic ratios of mineral pairs. The results show that our calculated results of temperatures for different

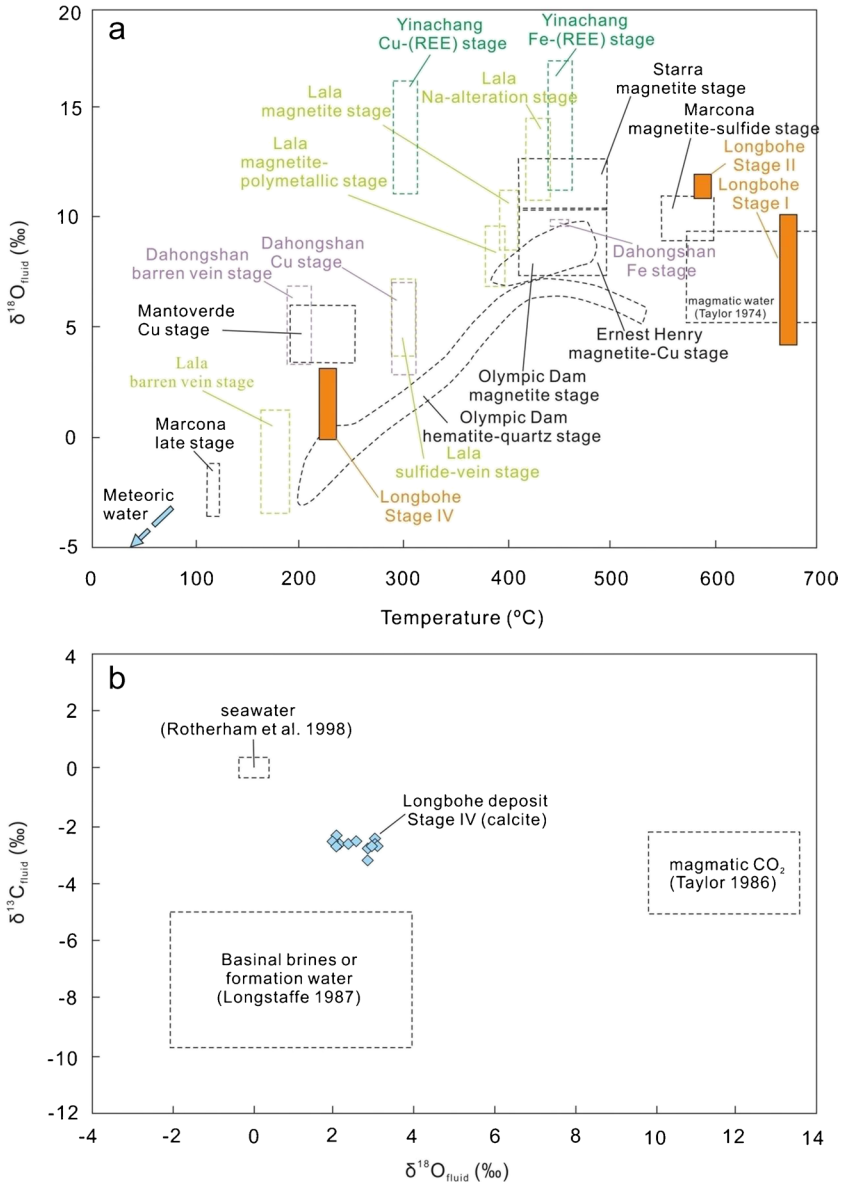

Fig. 15 **a** $\delta^{18}O$ versus temperature plots of the calculated fluids from various stages in the Longbohe deposit. Also shown are those of other IOCG deposits in the world (Williams et al. 2005, and references therein, Chen et al. 2011, Chen and Zhou 2012, Li et al. 2015, and Zhao et al. 2017). **b** $\delta^{13}C$ versus $\delta^{18}O$ plots of the calculated fluids of Stage IV in the Longbohe deposit

stages do not exhibit the expected homogenization as generally observed during high-temperatures metamorphism (e.g., Zheng et al. 1998, 1999). This feature suggests that the original isotopic equilibria broadly survived during late metamorphism in the shear zone, and thus the calculated temperatures could represent those of the Fe-Cu mineralization event in the Longbohe deposit.

Stage I is characterized by pervasive albite alteration. Although the temperature for this stage is not available, the almost identical mineral assemblages to that of Stage II suggests a broadly similar temperature for both stages (515 to 670 ºC), that in turn is consistent to the high temperature of up to 500 ºC as documented for the pre-ore sodic alteration in many IOCG systems (Perring et al. 2000; Oliver et al. 2004; Corriveau et al. 2016). Fluids of Stage I have $\delta^{18}O$ values (4.3 to 10.1 ‰) broadly similar to typical magmatic water (Fig. 15a), indicative of a major contribution of magmatic fluids. It is notable that two analyses with slightly higher values (e.g., 10.1 ‰) may suggest additional minor involvement of oxygen from high-$\delta^{18}O$ host rocks (e.g., sedimentary rocks) during fluid-rock interactions.

Stage II fluids have $\delta^{18}O$ values (10.8 to 11.7 ‰) slightly higher than those of Stage I, but broadly overlapping with those of the magnetite stage in some magmatic fluid-related IOCG deposits (Fig. 15a; e.g., Starra deposit, Rotherham et al. 1998). Such high values tend to suggest more contribution of oxygen from the host rocks, but magmatic fluids should still be the dominant source as supported by the high

temperatures of the fluids of up to 670 ºC. On the other hand, Stage III fluids have lower temperatures (332 to 402 ºC), but exhibit mantle-like $\delta^{34}S$ values (1.2 to 3.7 ‰; Seal 2006) that are broadly comparable to the Cu stage (magmatic in origin) of the Sin Quyen deposit (Fig. 14a; Li and Zhou 2018; Li et al. 2018a). These results strongly indicate that the fluids for the Cu mineralization are also magmatic in origin.

Stage IV veins are clearly undeformed, indicating that they postdate the deformed Fe-Cu mineralizing system defined by Stages I, II and III. The fluids of this stage have relatively low temperatures (~ 220 ºC; Cui 2007) and $\delta^{18}O$ values (-0.2 to 3.2 ‰; Fig. 15a), indicating possible contributions of both magmatic fluids and meteoric water. The magmatic contributions are also supported by the $\delta^{14}C$ values of the fluids (-3.2 to -2.3 ‰) that are similar to magmatic CO_2 (Fig. 15b; Taylor 1986), likely related to abundant Cenozoic (~ 30 Ma) magmatic rocks in the region (e.g., Cao et al. 2011; Liu et al. 2012, 2015). However, the $\delta^{34}S$ values exhibit a wide range (0.6 to 7.7 ‰) and bimodal distribution with two peaks at ~ 1.5 ‰ and ~ 6.0 ‰ (Fig. 14b), thus indicative of multiple sulfur sources. The former peak is comparable to typical magmatic sources or Stage III sulfides, likely indicating the involvement of magmatic sulfur or remobilization of sulfur of Stage III sulfides during the Cenozoic (~ 30 Ma) reactivation of the ASRR shear zone. Instead, the latter peak was possibly related to sulfate in sedimentary rocks (Taylor 1974) or even another pulse of high-$\delta^{34}S$ fluids, which need more investigation in the future.

Classification of the Longbohe deposit as an IOCG deposit

Although the Sin Quyen deposit in the LSQ belt was well constrained to be IOCG-like (e.g., McLean 2001; Li and Zhou 2018; Li et al. 2018a), the genetic affinity of the Longbohe deposit of the same belt is highly controversial. It was traditionally considered to be a VMS-type (Gao 2006) or superimposed SEDEX-type deposit (Yang et al. 1999; Zhang 2004; Cui et al. 2008), partially due to the strata-bound nature of the ore bodies or banded texture of some ores. Our study confirms that the Longbohe deposit shares mineralization styles and a paragenetic sequence with the Sin Quyen and other IOCG deposits worldwide (ESM Table 10). For example, the Longbohe deposit is of hydrothermal replacement origin, and exhibits a paragenetic sequence of early pervasive pre-ore Na alteration, followed by Fe mineralization with abundant low-Ti magnetite and late Cu mineralization, similar to the Sin Quyen deposit (Li and Zhou 2018). In addition to Fe and Cu, it also contains variable enrichment/mineralization of LREEs and P but is depleted in Pb, Zn or Ag, unlike the VMS- or SEDEX-type deposits previously considered (e.g., Franklin et al. 2005; Leach et al. 2005). In particular, magnetite of the Longbohe deposit has trace elemental compositions indistinguishable from those of the Sin Quyen deposit, and the Lala, Yinachang and Dahongshan deposits in the Kangdian IOCG province (Fig. 7), further supporting an IOCG affinity of the Longbohe deposit.

The timing and tectonic environment of the Longbohe–Sin Quyen Fe-Cu belt

The identification of the Longbohe deposit as an IOCG deposit allows us to propose that the Longbohe–Sin Quyen Fe-Cu belt could be a potentially important IOCG belt along the ASRR shear zone. Although the Sin Quyen deposit was well constrained to have formed at ~ 840 Ma, the timing of the Longbohe deposit was not precisely known so far. Our study identified two types of zircon from both Fe (Stage II) and Cu-dominated (Stage III) ores. Type 1 zircon grains in both samples exhibit well-developed oscillatory zoning and high Th/U ratios (mostly > 0.4; Fig. 12a), similar to typical magmatic zircon. In particular, their ages of 1710 ± 10 Ma and 904 ± 6 Ma (calculated by the youngest cluster of analyses; Fig. 11a, b) are comparable to the ages of the ~ 1.7 Ga meta-volcanic and ~ 0.9 Ga meta-sedimentary rocks of the hosting Longbohe Group, respectively (Liu and Chen 2019), further indicating that Type 1 zircons in both samples should be primary, magmatic zircon of the protoliths.

In contrast, Type 2 zircon grains in both samples exhibit similar internal textures and U–Pb ages that are remarkably different from Type 1 zircon (Figs. 10b, d and 11c, d). They have much younger ages of ~ 850 Ma, coeval with the Sin Quyen deposit and the regional subduction event lasting from ~ 850 to ~ 740 Ma (e.g., Qi et al. 2012, 2014, 2016; Cai et al. 2014, 2015; Wang et al. 2016; Li et al. 2018b). Thus, these zircons were likely of metamorphic origin related to the subduction event or hydrothermal in origin related to the Fe-Cu mineralization. In general, metamorphic zircon can form by: (1) crystallization from melt during anatexis (e.g., Roberts and Finger 1997; Vavra et al. 1999); (2) nucleation and crystallization due to release of Zr and Si by metamorphic breakdown of solidus minerals (e.g., Fraser et al. 1997; Bingen et al. 2001); (3) metamorphic recrystallization of protolith zircon (e.g., Hoskin and Black 2000; Hoskin and Schaltegger 2003); or (4) direct precipitation from metamorphic fluids (e.g., Rubatto and Hermann 2003) or alteration products of protolith zircon triggered by metamorphic fluids (e.g., Rizvanova et al. 2000; Corfu et al. 2003). The former three processes generally involve high-grade metamorphism,

and the resultant metamorphic zircon could inherit the Hf isotopic compositions of precursors (e.g., earlier zircon or primary protoliths). However, the remarkably different Hf isotopic compositions of the 850 Ma zircon to those of magmatic zircon in the protolith or the whole rock Hf isotopic compositions (with enriched values) strongly exclude the aforementioned three processes. Also, they cannot be metamorphic zircons precipitated from a common metamorphic fluid related to the 850 Ma subduction event. The reason is that the 850 Ma zircon grains from the Fe and Cu ores have remarkably different chemical and Hf isotopic compositions to each others (Figs. 12 and 13), rebutting for a common metamorphic fluid source. Instead, the close association of the 850 Ma zircon grains with hydrothermal minerals (e.g., amphibole, titanite, albite or quartz; Fig. 10g, h) widespread in the Fe or Cu ores, well correlate with the hydrothermal origin of the ~ 850 Ma ore-forming event in Longbohe. Such conclusion is further supported by the local presence of inclusions of hydrothermal minerals (such as amphibole and titanite) in these zircons (Fig. 10e, f).

In summary, our new dating results confirm that the Longbohe deposit is roughly coeval with the ~ 840 Ma Sin Quyen deposit. The new findings thus tightly constrain the nature of the LSQ Fe-Cu belt as a Neoproterozoic (850–840 Ma) IOCG metallogenic belt. It is notable that these deposits are spatially and temporally associated with numerous Neoproterozoic (~ 850 to ~ 740 Ma) igneous rocks distributed along the ASRR shear zone. These igneous rocks were documented to similarly exhibit geochemical affinities of arc magmatism, and were confirmed to be part of the giant Neoproterozoic arc in the western Yangtze Block before its displacement by the Cenozoic ASRR shear zone (Fig. 1b; Qi et al. 2012, 2014; Cai et al. 2014, 2015; Wang et al. 2016; Li et al. 2018b). Considering that the 850–840 Ma arc magmatism in the ASRR shear zone and the western Yangtze Block has formed in a subduction setting (Zhao et al. 2018 and references therein), we propose that the Neoproterozoic Longbohe–Sin Quyen IOCG belt has formed in a subduction-related tectonic setting.

Incursion of external REE-rich fluids during Cu mineralization

This study confirmed that the fluids for both the Fe and Cu mineralization (i.e., Stages II and III) of the Longbohe deposit are dominantly magmatic in origin. However, the hydrothermal zircon grains for both stages do not show the coherent Hf isotopic compositions (Fig. 13b). Such a discrepancy implies that the fluids responsible for the Fe and Cu mineralization may have involved different pulses of magmas, or derive from a common magmatic fluid that interacted with different country rocks of distinct Hf isotopic compositions. The latter possibility could be excluded, because the hydrothermal zircon from both the Fe and Cu mineralization exhibit Hf isotopic ratios, remarkably different from those of various country rocks or the primary magmatic zircon hosted in these rocks, regardless of the mata-volcanic or meta-sedimentary hosting rocks (Fig. 13). Moreover, the mantle-like O-S isotopic features of both Fe and Cu mineralization do not show any signs of significant contributions of the wall rocks particularly the sedimentary units (Figs. 14 and 15), which are commonly of heavy S isotopic values. We thus propose that the varying Hf isotopic compositions of the hydrothermal zircon associated with Fe and Cu mineralization should be related to different magmatic sources of the ore-forming fluids.

In order to constrain the potential magmatic sources, we compare the ores with the regional coeval magmatism in terms of Hf isotopic ratios. Neoproterozoic arc magmatism lasting from ~ 850 to ~ 740 Ma is widely distributed in the ASRR shear zone, which were confirmed to be part of the giant Neoproterozoic arc belt in the western Yangtze Block before being displaced into the Cenozoic ASRR shear zone (Fig. 1b; Qi et al. 2012, 2014, 2016; Cai et al. 2014, 2015; Wang et al. 2016; Li et al. 2018b). Available data show that the mafic intrusions of ~ 850 Ma in the arc belt have $\varepsilon_{Hf(t)}$ values of 5.4 to 14.6 (Meng et al. 2015). On the other hand, Hf isotopic data of ~ 850 Ma felsic intrusions are currently not available, and thus the Hf isotopic ratios (-13.3 to 1.3; Li et al. 2018b; Chen et al. 2019) of slightly younger, ~ 830 Ma felsic intrusions in the region were used instead by assuming that both intrusions (~ 850 and ~ 830 Ma) have comparable Hf isotopic compositions. Such an assumption is reliable, because Neoproterozoic felsic magmatism lasting from ~ 850 to ~ 740 Ma are indeed geochemically similar, and are products of a common subduction-related event in the region (Qi et al. 2012, 2014, 2016; Cai et al. 2014, 2015; Wang et al. 2016; Li et al. 2018b). Further comparison show that the hydrothermal zircon grains of Fe stage have high $\varepsilon_{Hf(t)}$ values (7.5 to 12.7) similar to those of the mafic intrusions (5.4 to 14.6) in the region (Fig. 13b, c), while those of Cu stage has $\varepsilon_{Hf(t)}$ values (0.3 to 4.0) much lower than the Fe stage, but slightly higher than and partially overlap with those of the felsic intrusions (-13.0 to 1.3) in the region (Fig. 13b, c). The comparison indicates that the fluids for the Fe mineralization were likely sourced from the mafic magmas, whereas those for the Cu mineralization involved an external, felsic magma-derived fluid which has mixed with the evolved magmatic fluids from the Fe mineralization. It is notable that the hydrothermal zircon of the Cu stage has remarkably elevated LREE contents comparable to those of the Fe stage (Fig. 12c,

d), indicating that the external, magmatic fluids were relatively LREE-rich. The incursion of the external REE-rich fluids should be responsible for the precipitation of LREE-rich allanite in the Cu stage, an interpretation that is supported by the $\varepsilon_{Nd(t)}$ values of allanite (-6.1 to -3.1 at 850 Ma) which are similar to those of the felsic intrusions (-11.9 to 0.0), but different from those of the mafic intrusions (0.4 to 6.2) or the country rocks (4.2 to 7.3 at 850 Ma) in the region (Liu 2022). Such a model involving both mafic magma-derived fluids and external fluids with isotopic signatures mimicking felsic magmas has been also documented in other hydrothermal deposits, such as the Lala IOCG deposit (Chen et al. 2014) and the Black Mountain porphyry Cu-Au deposit (Cao et al. 2020).

General implications

Implication for Fe-Cu metallogeny in the ASRR shear zone

On the basis of similar ore-hosting rocks and Proterozoic intrusions, the LSQ Fe-Cu belt was previously considered to be part of the Kangdian IOCG metallogenic province before being displaced into the ASRR shear zone (Zhao and Zhou 2011; Zhou et al. 2014). However, our study did not obtain the expected old ages for the IOCG mineralization events (e.g., the ~ 1.66 and ~ 1.08 Ga major mineralization events) as documented in the Kangdian province (e.g., Chen and Zhou 2012; Zhao et al. 2013, 2017). Instead, 850–840 Ma documented in the Kangdian IOCG province was constrained to represent hydrothermal overprinting/mobilization events (Chen and Zhou 2012, 2014; Zhao et al. 2013, 2017; Li and Zhou 2015). Such an age inconsistency thus challenges the possible linkage between the LSQ belt and the Kangdian IOCG metallogenic province. However, it is important to note that in addition to the similar Proterozoic geologies, a number of Phanerozoic lithologies in the ASRR shear zone were also documented to be comparable to those in the Kangdian region or more broadly, the western Yangtze Block. Typical examples are late Permian (~ 260 Ma) basalts and rhyolites, as well as magmatic oxide (e.g., Mianhuadi in South China) and sulfide (e.g., Ban Phuc in Vietnam) deposits, which are well confirmed to be initially parts of the Emeishan plume in the western Yangtze Block before being displaced into the shear zone (Zhou et al. 2013; Wang et al. 2018; Xu et al. 2019; Shellnutt et al. 2020). These lines of evidence are in favor of model that the Neoproterozoic LSQ belt could be part of the Kangdian IOCG province (Zhou et al. 2014). We speculate that the older ~ 1.66 and ~ 1.08 Ga mineralization events in the Kangdian province are also likely available in the ASRR shear zone but not yet discovered due to the current low exploration level and a lack of sufficient dating results. It is believed that future exploration, particularly in the southern part of the ASRR shear zone (e.g., the part between Dahongshan and Sin Quyen), will provide more constraints on this possibility.

Implication for diverse IOCG systems

Our identification of the Neoproterozoic LSQ IOCG belt as a subduction-related IOCG belt allows us to make a comparison with other settings and thus to understand the diversity of IOCG systems. Firstly, compared to Precambrian intracontinental IOCG deposits worldwide, the LSQ IOCG belt tends to exhibit slightly different features (ESM Table 10). For example, the REE mineralization in the LSQ IOCG belt is dominated by REE-silicates (e.g., allanite), different from most others formed in Precambrian intra-continental IOCG deposits in which REE occur as REE fluorocarbonates, or phosphates with minor REE silicates (e.g., Kangdian province; Chen and Zhou 2014, 2015; Li and Zhou 2015). Such a difference may result from the high Si, Al, Ca and Cl but low F activities of the ore-forming fluids, which is evident by the common presence of Cl-rich amphibole and biotite but rare appearance of fluorite in the Longbohe and Sin Quyen deposits (e.g., Li and Zhou 2018). Despite not exclusive, such a relatively F-poor but Cl-rich nature of magmatic fluid tends to be more common in subduction-related systems (e.g., Wallace 2005), whereas the magmas and the related fluids from intra-continental rifting setting could be generally enriched in F (e.g., Zhang et al. 2022). Secondly, Precambrian intracontinental or subduction-related IOCG deposits tend to have relatively diverse metal associations (e.g., REE, U, Ag, Co, Mo, and Nb) in addition to Fe and Cu when compared to Phanerozoic subduction-related ones (e.g., the Central Andean belt) (ESM Table 10), possibly related to the metal-enriched nature of relatively ancient host rocks (e.g., Chen and Zhou 2015; Liu et al. 2021). In such case, the LSQ belt is able to be distinguishable from the Phanerozoic examples by the remarkable enrichments of REEs (ESM Table 10), possibly ascribed to the different sources of the ore-forming fluids (e.g., REE-rich felsic magmas).

However, there are only a few subduction-related IOCG belts currently identified. Their rarity in the Precambrian can be, at least partially, ascribed to long-term uplift-denudation leading to poor preservation (e.g., porphyry systems; Wilkinson and Kesler 2007; Richards and Mumin 2013). Available studies have shown that Phanerozoic subduction-related IOCG deposits formed at depths generally less than 5 km (Barton 2014). Considering the high denudation rates in convergent belts (e.g., ~ 4.6 to 56.5 m/Ma; Schaller et al. 2018), most Precambrian IOCG deposits in convergent margins have a small chance of preservation. Thus, the rarity of Precambrian subduction-related IOCG deposits could be partially a function of erosion-preservation, in a scenario similar to porphyry Cu system.

Conclusions

The ~ 850 Ma Longbohe Fe-Cu-(LREE) deposit in the northwestern section of the LSQ Fe-Cu belt displays early Na alteration (I), Fe (II) and late Cu (III) mineralization stages that are comparable to the coeval Sin Quyen IOCG deposit in the same belt. Mineral assemblages of Stages I, II and III are variably metamorphosed and foliated, and are locally crosscut by abundant, post-deformational Cu-mineralized veins (Stage IV). Both Fe and Cu mineralization mainly formed from high- to medium-temperature (332 to 670 ℃) magmatic fluids. However, Hf isotopic compositions of hydrothermal zircon for the Fe and Cu stages imply that the magmatic fluids responsible for the Fe mineralization were derived from coeval mafic intrusions, whereas the Cu mineralization was related to the incursion of additional, external REE-rich fluids derived from coeval felsic magmas. This study confirms that the Longbohe–Sin Quyen Fe-Cu belt is a Neoproterozoic (850–840 Ma) IOCG belt formed in a subduction-related setting. The belt has features (e.g., enrichments of REEs as allanite) that are slightly different from other Precambrian intra-continental and Phanerozoic subduction-related IOCG deposits. The rarity of subduction-related IOCGs in the Precambrian is attributed to the poor preservation of potential deposits in convergent belts, similar to copper porphyry systems.

Supplementary Information The online version contains supplementary material available at https://doi.org/10.1007/s00126-023-01198-4.

Acknowledgements We would like to thank Dr. Chengbiao Leng and Ronglin Ma for their help during field work. Dr. Jianfeng Gao, Yanwen Tang, Youwei Chen, Zhihui Dai, Jing Gu and Mr. Xiang Li from Institute of Geochemistry, Chinese Academy of Sciences and Dr. Kaiyun Chen from Northwest University (China) are thanked for their help with data collection. This manuscript was profoundly improved thanks to the constructive comments by two anonymous reviewers, and editorial handling by Prof. Bernd Lehmann and Prof. Ruizhong Hu.

Funding This study was supported by the National Natural Science Foundation of China (42121003, U2202210) and the West Light Foundation of Chinese Academy of Sciences (Grant No. xbzg-zdsys-202205).

Declarations

Conflict of interest The authors declare no competing interests.

References

Bao ZA, Chen L, Zong CL, Yuan HL, Chen KY, Dai MN (2017) Development of pressed sulfide powder tablets for *in situ* sulfur and lead isotope measurement using LA-MC-ICP-MS. Int J Mass Spectrom 421:255–262

Barton MD (2014) Iron oxide (-Cu-Au-REE-P-Ag-U-Co) systems. In: Holland HD, Turekian KK (eds) Treatise on Geochemistry, 2nd edn. Elsevier, Oxford, pp 515–541

Bingen B, Austrheim H, Whitehouse M (2001) Ilmenite as a source for zirconium during high-grade metamorphism? Textural evidence from the Caledonides of Western Norway and implications for zircon geochronology. J Petrol 42:355–375

Cai YF, Wang YJ, Cawood PA, Fan WM, Liu HC, Xing XW, Zhang YZ (2014) Neoproterozoic subduction along the Ailaoshan zone, South China: Geochronological and geochemical evidence from amphibolites. Precambrian Res 245:13–28

Cai YF, Wang YJ, Cawood PA, Zhang YZ, Zhang AM (2015) Neoproterozoic crustal growth of the Southern Yangtze Block: Geochemical and zircon U-Pb geochronological and Lu-Hf isotopic evidence of Neoproterozoic diorite from the Ailaoshan zone. Precambrian Res 266:137–149

Cao MJ, Hollings P, Evans NJ, Cooke DR, McInnes BIA, Zhao KD, Qin KZ, Li DF, Sweet G (2020) *In situ* elemental and Sr isotope characteristics of magmatic to hydrothermal minerals from the Black Mountain porphyry deposit, Baguio District, Philippines. Econ Geol 115:927–944

Cao SY, Liu JL, Leiss B, Neubauer F, Genser J, Zhao CQ (2011) Oligo-Miocene shearing along the Ailao Shan-Red River shear zone: Constraints from structural analysis and zircon U/Pb geochronology of magmatic rocks in the Diancang Shan massif, SE Tibet, China. Gondwana Res 19:975–993

Chen HY, Kyser TK, Clark AH (2011) Contrasting fluids and reservoirs in the contiguous Marcona and Mina Justa iron oxide-Cu (-Ag-Au) deposits, south-central Perú. Miner Deposita 46:677–706

Chen WT, Zhou MF (2012) Paragenesis, stable isotopes, and molybdenite Re-Os isotope age of the Lala copper deposit, southwest China. Econ Geol 107:459–480

Chen WT, Zhou MF (2014) Ages and compositions of primary and secondary allanite from the Lala Fe-Cu deposit, SW China: implications for multiple episodes of hydrothermal events. Contrib Mineral Petrol 168:1043

Chen WT, Zhou MF, Gao JF (2014) Constraints of Sr isotopic compositions of apatite and carbonates on the origin of Fe and Cu mineralizing fluids in the Lala Fe-Cu-(Mo, LREE) deposit, SW China. Ore Geol Rev 61:96–106

Chen WT, Zhou MF (2015) Mineralogical and geochemical constraints on mobilization and mineralization of rare earth elements in the Lala Fe-Cu-(Mo, REE) deposit, SW China. Am J Sci 315:671–711

Chen WT, Zhou MF, Gao JF, Hu RZ (2015) Geochemistry of magnetite from Proterozoic Fe-Cu deposits in the Kangdian metallogenic province, SW China. Miner Deposita 50:795–809

Chen WT, Zhou MF, Tang YW (2022) New insights about the origin of the Shilu Fe-Cu-Co deposit, Hainan Island, South China, with emphasis on the regional metallogeny. Miner Deposita 57:1415–1430

Chen XY, Liu JL, Fan WK, Qi YC, Wang W, Chen JF, Burg JP (2017) Neoproterozoic granitoids along the Ailao Shan-Red River belt: Zircon U-Pb geochronology, Hf isotope analysis and tectonic implications. Precambrian Res 299:244–263

Chen XY, Burg JP, Liu JL, Qi YC, Fan WK, Wang K (2019) Multistage remobilization of the southwestern margin of the South China plate: Insights from zircon U-Pb geochronology and Hf isotope of granitic rocks from the Yao Shan complex, southeastern Tibet Plateau. Tectonics 38:621–640

Chung SL, Lee TY, Lo CH, Wang PL, Chen CY, Yem NT, Hoa TT, Wu GY (1997) Intraplate extension prior to continental extrusion along the Ailao Shan-Red River shear zone. Geology 25:311–314

Clayton RN, Mayeda TK (1963) The use of bromine pentafluoride in the extraction of oxygen from oxides and silicates for isotopic analysis. Geochim Cosmochim Acta 27:43–52

Coplen TB, Kendall C, Hopple J (1983) Comparison of stable isotope reference samples. Nature 302:236–238

Corfu F, Hanchar JM, Hoskin PWO, Kinny P (2003) Atlas of zircon textures. Rev Mineral Geochem 53:469–495

Corriveau L, Montreuil JF, Potter EG (2016) Alteration facies linkages among iron oxide copper-gold, iron oxide-apatite, and affiliated deposits in the Great Bear magmatic zone, Northwest Territories, Canada. Econ Geol 111:2045–2072

Cui YL (2007) The synthetic information prognosis of metallogenic prospecting and volcanic mineralization of Longbohe copper deposit in Jinping County of Yunnan Province: PhD thesis, Kunming, China, Kunming University of Science and Technology, 1–362 (in Chinese with English abstract)

Cui YL, Jiang SD, Chen YG (2008) Ore-forming fluids of the Longbohe copper deposit in Jinping, Yunnan. Geol Prospect 44:55–61 ((in Chinese with English abstract))

Duong VH, Trinh PT, Nguyen TD, Piestrzyski A, Nguyen DC, Pieczonka J, Ngo XD, Van PT, Pham BT, Nguyen-Van H, Van LN, Bui DT, Khac DV, Bui CT (2021) Cu-Au mineralization of the Sin Quyen deposit in north Vietnam: A product of Cenzoic left-lateral movement along the Red River shear zone. Ore Geol Rev 132:104065. https://doi.org/10.1016/j.oregeorev.2021.104065

Faure M, Lepvrier C, Nguyen VV, Vu TV, Lin W, Chen ZC (2014) The South China block-Indochina collision: Where, when and how? J Asian Earth Sci 79:260–274

Franklin JM, Gibson HL, Jonasson IR, Galley AG (2005) Volcanogenic massive sulfide deposits. Econ Geol 100: 523–560

Fraser G, Ellis D, Eggins S (1997) Zirconium abundance in granulite-facies minerals, with implications for zircon geochronology in high-grade rocks. Geology 25:607–610

Gao J (2006) Discussion ore genesis and prospecting direction of the east Longbohe copper ore belt of Yunnan. Geol Prospect 42:12–16 ((in Chinese with English abstract))

Gong W, Jiang XD (2017) Thermal evolution history and its genesis of the Ailao Shan-Red River fault zone in the Ailao Shan and Day Nui Con Voi massif during Oligocene-Early Miocene. Earth Sci 42:223–239 ((in Chinese with English abstract))

Groves DI, Bierlein FP, Meinert LD, Hitzman MW (2010) Iron oxide copper-gold (IOCG) deposits through Earth history: Implications for origin, lithospheric setting, and distinction from other epigenetic iron oxide deposits. Econ Geol 105:641–654

Hieu PT, Chen FK, Zhu XY, Wang W, Nguyen TBT, Bui MT, Nguyen QL (2009) Zircon U-Pb ages and Hf isotopic composition of the Posen granite in northwestern Vietnam. Acta Petrol Sin 25:3141–3152 ((in Chinese with English abstract))

Hieu PT, Chen FK, Zhu XY, Wang F (2010) Zircon ages of paragneisses from the Sinh Quyen Formation in northwestern Vietnam and their geological significances. Earth Sci: J China U Geosci 35:201–210 ((in Chinese with English abstract))

Hieu PT, Chen FK, Me LH, Thuy NTB, Siebel W, Lan TG (2012) Zircon U-Pb ages and Hf isotopic compositions from the Sin Quyen Formation: the Precambrian crustal evolution of northwest Vietnam. Int Geol Rev 54:1548–1561

Hitzman MW, Oreskes N, Eianudi T (1992) Geological characteristics and tectonic setting of Proterozoic iron oxide (Cu-U- Au-REE) deposits. Precambrian Res 58:241–287

Hitzman MW (2000) Iron oxide-Cu-Au deposits: what, where, when, and why. In: Porter TM (ed) Hydrothermal iron oxide copper-gold and related deposits: a global perspective, 1. PGC Publishing, Adelaide, pp 9–25

Hitzman MW, Valenta RK (2005) Uranium in iron oxide-copper-gold (IOCG) systems. Econ Geol 100:1657–1661

Hoskin PWO, Black LP (2000) Metamorphic zircon formation by solid-state recrystallization of protolith igneous zircon. J Metamorph Geol 18:423–439

Hoskin PWO, Schaltegger U (2003) The composition of zircon and igneous and metamorphic petrogenesis. Rev Mineral Geochem 53:27–55

Ji L, Liu FL, Wang F, Cai J, Wang W, Tian ZH, Liu LS (2017) Ployphase metamorphism in Diancang Shan-Ailao Shan complex zone: Constraints from U-Pb dating and trace elements of zircons in metasedimentary rocks, Gasa area. Acta Petrol Sin 33:605–621 ((in Chinese with English abstract))

Leach DL, Sangster DF, Keller KD, Large RR, Garven G, Allen CR, Gutzmer J, Walters S (2005) Sediment-hosted lead-zinc deposits: A global perspective. Econ Geol 100:561–608

Leloup PH, Kienast JR (1993) High-temperature metamorphism in a major strike-slip shear zone: the Ailao Shan-Red River, People's Republic of China. Earth Planet Sci Lett 118:213–234

Leloup PH, Lacassin R, Tapponnier P, Schärer U, Zhong DL, Liu XH, Zhang LS, Ji SC, Trinh PT (1995) The Ailao Shan-Red River shear zone (Yunnan, China), Tertiary transform boundary of Indochina. Tectonophysics 251:3–84

Li BL, Ji JQ, Fu XY, Gong JF, Song B, Qing JC, Zhang C (2008) Zircon SHRIMP dating and its geological implications of the metamorphic rocks in Ailao Shan-Diancang mountain ranges, west Yunnan. Acta Petrol Sin 24:2322–2330 ((in Chinese with English abstract))

Li BL, Ji JQ, Fu XY, Gong JF, Song B, Qing JC, Zhang C, Ma ZJ (2009) Metamorphic time limits' study on the metamorphic rocks series of Ailao Shan-Diancang mountain ranges, west Yunnan. Acta Petrol Sin 25:595–608 ((in Chinese with English abstract))

Li XC, Zhou MF (2015) Multiple stages of hydrothermal REE remobilization recorded in fluorapatite in the Paleoproterozoic Yinachang Fe-Cu-(REE) deposit, Southwest China. Geochim Cosmochim Acta 166:53–73

Li XC, Zhao XF, Zhou MF, Chen WT, Chu ZY (2015) Fluid inclusion and isotope constraints on the origin of the Paleoproterozoic Yinachang Fe-Cu-(REE) deposit, southwest China. Econ Geol 110:1339–1369

Li XC, Zhou MF (2018) The nature and origin of hydrothermal REE mineralization in the Sin Quyen deposit, northwestern Vietnam. Econ Geol 113:645–673

Li XC, Zhou MF, Chen WT, Zhao XF, Tran MD (2018a) Uranium-lead dating of hydrothermal zircon and monazite from the Sin Quyen Fe-Cu-REE-Au-(U) deposit, northwestern Vietnam. Miner Deposita 53:399–416

Li XC, Zhao JH, Zhou MF, Gao JF, Sun WH, Tran MD (2018b) Neoproterozoic granitoids from the Phan Si Pan belt, northwest Vietnam: Implication for the tectonic linkage between northwest Vietnam and the Yangtze Block. Precambrian Res 309:212–230

Li XC, Zhou MF, Yang YH, Zhao XF, Gao JF (2018c) Disturbance of the Sm-Nd isotopic system by metasomatic alteration: A case study of fluorapatite from the Sin Quyen Cu-LREE-Au deposit, Vietnam. Am Miner 103:1487–1496

Liu FG, Liu X, Cheng P, Zeng QR (2005) The establishment of Proterozoic Longbohe rock Group in Longbohe area, Jinping. Yunnan Geol 24:414–420 ((in Chinese with English abstract))

Liu JL, Tang Y, Tran MD, Cao SY, Zhao L, Zhang ZC, Zhao ZD, Chen W (2012) The nature of the Ailao Shan-Red River (ASRR) shear zone: Constraints from structural, microstructural and fabric analyses of metamorphic rocks from the Diancang Shan, Ailao Shan and Day Nui Con Voi massifs. J Asian Earth Sci 47:231–251

Liu JL, Chen XY, Wu WB, Tang Y, Tran MD, Nguyen QL, Zhang ZC, Zhao ZD (2015) New tectono-geochronological constraints on timing of shearing along the Ailao Shan-Red River shear zone: Implications for genesis of Ailao Shan gold mineralization. J Asian Earth Sci 103:70–86

Liu L, Chen WT (2019) Geology, mineralization styles and age of ore-hosting rocks of the Proterozoic Longbohe-Sin Quyen Fe-Cu belt: Implications for regional metallogeny. Ore Geol Rev 111:103013. https://doi.org/10.1016/j.oregeorev.2019.103013

Liu L, Zhang W, Jin C, Chen WT (2021) Mineralogical and geochemical constraints on the origin of the variable REE enrichments in the Kangdian IOCG province, SW China. Ore Geol Rev 138:104381. https://doi.org/10.1016/j.oregeorev.2021.104381

Liu L (2022) Geology, geochemical characteristics and genesis of the Longbohe Fe-Cu-REE deposit, SW China and its regional metallogenic significance: PhD thesis, Beijing, China, University of Chinese Academy of Sciences, 1–246 (in Chinese with English abstract)

Liu YS, Hu ZC, Gao S, Günther D, Xu J, Gao CG, Chen HH (2008) *In situ* analysis of major and trace elements of anhydrous minerals by LA-ICP-MS without applying an internal standard. Chem Geol 257:34–43

Liu YS, Hu ZC, Zong KQ, Gao CG, Gao S, Xu J, Chen HH (2010) Reappraisement and refinement of zircon U-Pb isotope and trace element analyses by LA-ICP-MS. Chin Sci Bull 55:1535–1546

Longstaffe FJ (1987) Stable isotope studies of diagenetic processes. Mineral Assoc Can Short Course 13:187–257

Ludwig KR (2003) Isoplot 3.00: A geochronological toolkit for Microsoft Excel. Berkeley Geochronology Center, Berkeley, p 70

Machado N, Simonetti A (2001) U-Pb dating and Hf isotopic composition of zircon by laser-ablation-MC-ICP-MS. In: Sylvester PJ (ed) Laser ablation-ICPMS in the Earth sciences. Principles and applications. Mineralogical Association of Canada, Ottawa, pp 121–146

McDonough WF, Sun SS (1995) The composition of the Earth. Chem Geol 120:223–253

McLean RN (2001) The Sin Quyen iron oxide-copper-gold-rare earth oxide mineralization of North Vietnam. In: Porter TM (ed) Hydrothermal iron oxide copper-gold and related deposits: A global perspective, vol 2. PGC Publishing, Adelaide, pp 293–301

Meng E, Liu FL, Du LL, Liu PH, Liu JH (2015) Petrogenesis and tectonic significance of the Baoxing granitic and mafic intrusions, southwestern China: Evidence from zircon U-Pb dating and Lu-Hf isotopes, and whole-rock geochemistry. Gondwana Res 28:800–815

Mudd GM, Weng Z, Jowitt SM, Turnbull ID, Graedel TE (2013) Quantifying the recoverable resources of by-product metals: The case of cobalt. Ore Geol Rev 55:87–98

Ngo XD, Zhao XF, Tran TH, Deng XD, Li JW (2020) Two episodes of REEs mineralization at the Sin Quyen IOCG deposit, NW Vietnam. Ore Geol Rev 125:103676. https://doi.org/10.1016/j.oregeorev.2020.103676

Ohmoto H (1972) Systematics of sulfur and carbon isotopes in hydrothermal ore deposits. Econ Geol 67:551–578

Ohmoto H, Rye RO (1979) Isotopes of sulfur and carbon. In: Barnes HL (ed) Geochemistry of hydrothermal ore deposits, 2nd edn. Wiley, New York, pp 509–567

Oliver NHS, Cleverley JS, Mark G, Pollard PJ, Fu B, Marshall LJ, Rubenach MJ, Williams PJ, Baker T (2004) Modeling the role of sodic alteration in the genesis of iron oxide-copper-gold deposits, Eastern Mount Isa Block, Australia. Econ Geol 99:1145–1176

Perring CS, Pollard JP, Dong G, Nunn AJ, Blake KL (2000) The Lightning Greek sill complex, Cloncurry district, northwest Queensland: A source of fluids for Fe oxide Cu-Au mineralization and sodic-calcic alteration. Econ Geol 95:1067–1089

Qi XX, Zeng LS, Zhu LH, Hu ZC, Hou KJ (2012) Zircon U-Pb and Lu-Hf isotopic systematic of the Daping plutonic rocks: Implications for the Neoproterozoic tectonic evolution of the northeastern margin of the Indochina block, Southwest China. Gondwana Res 21:180–193

Qi XX, Santosh M, Zhu LH, Zhao YH, Hu ZC, Zhang C, Ji FB (2014) Mid-Neoproterozoic arc magmatism in the northeastern margin of the Indochina block, SW China: Geochronological and petrogenetic constraints and implications for Gondwana assembly. Precambrian Res 245:207–224

Qi XX, Santosh M, Zhao YH, Hu ZC, Zhang C, Ji FB, Wei C (2016) Mid-Neoproterozoic ridge subduction and magmatic evolution in the northeastern margin of the Indochina block: Evidence from geochronology and geochemistry of calc-alkaline plutons. Lithos 248–251:138–152

Richards JP, Mumin AH (2013) Magmatic-hydrothermal processes within an evolving Earth: Iron oxide-copper-gold and porphyry Cu±Mo±Au deposits. Geology 41:767–770

Rizvanova NG, Levchenkov OA, Belous AE, Bezmen NI, Maslenikov AV, Komarov AN, Makeev AF, Levskiy LK (2000) Zircon reaction and stability of the U-Pb isotope system during the interaction with carbonate fluid: Experimental hydrothermal study. Contrib Mineral Petrol 139:101–134

Roberts M, Finger F (1997) Do U-Pb zircon ages from granulites reflect peak metamorphic conditions? Geology 25:319–322

Rotherham JF, Blake KL, Carwright I, Williams PJ (1998) Stable isotope evidence for the origin of the Mesoproterozoic Starra Au-Cu deposit, Cloncurry district, northwest Queensland. Econ Geol 93:1435–1449

Rubatto D, Hermann J (2003) Zircon formation during fluid circulation in eclogites (Monviso, Western Alps): Implications for Zr and Hf budget in subduction zones. Geochim Cosmochim Acta 67:2173–2187

Schaller M, Ehlers TA, Lang KAH, Schmid M, Fuentes-Espoz JP (2018) Addressing the contribution of climate and vegetation cover on hillslope denudation, Chilean Coastal Cordillera (26°-38° S). Earth Planet Sci Lett 489:111–122

Seal RR (2006) Sulfur isotope geochemistry of sulfide minerals. Rev Mineral Geochem 61:633–677

Searle MP (2006) Role of the Red River shear zone, Yunnan and Vietnam, in the continental extrusion of SE Asia. J Geol Soc London 163:1025–1036

Searle MP, Yeh MW, Lin TH, Chung SL (2010) Structural constraints on the timing of left-lateral shear along the Red River shear zone in the Ailao Shan and Dicang Shan ranges, Yunnan, SW China. Geosphere 6:316–338

Shellnutt JG, Pham TT, Denyszyn SW, Yeh MW, Tran TA (2020) Magmatic duration of the Emeishan large igneous province: Insights from northern Vietnam. Geology 48:457–461

Tapponnier P, Lacassin R, Leloup PH, Schärer U, Zhong DL, Wu HW, Liu XH, Ji SC, Zhang LS, Zhong JY (1990) The Ailao Shan/Red River metamorphic belt: Tertiary left-lateral shear between Indochina and South China. Nature 343:431–437

Taylor BE (1986) Magmatic volatiles: Isotopic variation of C, H and S. Rev Mineral Geochem 16:185–271

Taylor HP Jr (1974) The application of oxygen and hydrogen isotope studies to problems of hydrothermal alteration and ore deposition. Econ Geol 69:843–883

Tran TT (2011) Meso-Neoarchean supersequence. In: Nguyen KS (ed) Geology and Earth resources of Vietnam. Publishing House for Science and Technology, Hanoi, p 38–46

Usuki T, Lan CY, Tran TH, Pham TD, Wang KL, Shellnutt GJ, Chung SL (2015) Zircon U-Pb ages and Hf isotopic compositions of alkaline silicic magmatic rocks in the Phan Si Pan-Tu Le region, northern Vietnam: Identification of a displaced western extension of the Emeishan Large Igneous Province. J Asian Earth Sci 97:102–124

Vavra G, Schmid R, Gebauer D (1999) Internal morphology, habit and U-Th-Pb microanalysis of amphibole to granulite facies zircon: Geochronology of the Ivren Zone (Southern Alps). Contrib Mineral Petrol 134:380–404

Vervoort JD, Patchett PJ, Söderlund U, Baker M (2004) Isotopic composition of Yb and the determination of Lu concentrations and Lu/Hf ratios by isotope dilution using MC-ICPMS. Geochem Geophys Geosyst 5:1–15

Wallace PJ (2005) Volatiles in subduction zone magmas: concentrations and fluxes based on melt inclusion and volcanic gas data. J Volcanol Geotherm Res 140:217–240

Wang CY, Wei B, Zhou MF, Minh DH, Qi L (2018) A synthesis of magmatic Ni-Cu-(PGE) sulfide deposits in the ~260 Ma Emeishan large igneous province, SW China and northern Vietnam. J Asian Earth Sci 154:162–186

Wang DB, Tang Y, Liao SY, Yin FG, Sun ZM, Wang LQ, Wang BD (2013) Zircon U-Pb dating and its geological implications of the metamorphic rock series in Ailao Shan ranges, western Yunnan. Acta Petrol Sin 29:1261–1278 ((in Chinese with English abstract))

Wang YJ, Zhou YZ, Cai YF, Liu HC, Zhang YZ, Fan WM (2016) Geochronological and geochemical constraints on the petrogenesis of the Ailaoshan granitic and migmatite rocks and its implications on Neoproterozoic subduction along the SW Yangtze Block. Precambrian Res 283:106–124

Weng ST (2014) Cenozoic deformation characteristics and regional tectonic thermal evolution discussion of Yaoshan metamorphic complex in the west of Yunnan: MS thesis, China, China University of Geosciences (Beijing), 1–53 (in Chinese with English abstract)

Weng ZH, Jowitt SM, Mudd GM, Haque N (2015) A detailed assessment of global rare earth element resources: Opportunities and challenges. Econ Geol 110:1925–1952

Wilkinson BH, Kesler SE (2007) Tectonism and exhumation in convergent margin orogens: Insights from ore deposits. J Geol 115:611–627

Williams PJ, Barton MD, Johnson DA, Fontboté L, Haller AD, Mark G, Oliver NHS (2005) Iron oxide copper-gold deposits: Geology, space-time distribution, and possible modes of origin. Econ Geol 100:371–405

Wu HJ (2012) Pyrometamorphism and ultrahigh-temperature metamorphism deformation and tectonic implication of the Day Nui Con Voi in the northwestern Vietnam and Yaoshan Group in western Yunnan: MS thesis, China, China University of Geosciences (Beijing), 1–54 (in Chinese with English abstract)

Xu J, Xia XP, Lai CK, Zhou ML, Ma PF (2019) First identification of late Permian Nb-enriched basalts in Ailaoshan region (SW Yunnan, China): Contribution from Emeishan plume to subduction of eastern Paleotethys. Geophys Res Lett 46:2511–2523

Yang JF, Liu JS, Liu HT (1999) Geology and metal genesis of the Laoxinjie copper deposit in the Longbohe ore belt, Yunnan. Geol Explor Non-Ferrous Met 8:470–475 ((in Chinese with English abstract))

Yuan HL, Liu X, Chen L, Bao ZA, Che KY, Zong CL, Li XC, Qiu JWH (2018) Simultaneous measurement of sulfur and lead isotopes in sulfides using nanosecond laser ablation coupled with two multi-collector inductively coupled plasma mass spectrometers. J Asian Earth Sci 154:386–396

Zhai MG, Cong BL, Qiao GS, Zhang RA (1990) Sm-Nd and Rb-Sr geochronology of metamorphic rocks from SW Yunnan orogenic zones, China. Acta Petrol Sin 6:1–11 ((in Chinese with English abstract))

Zhang LH (2004) Research on the mineralization of Laoxinjie copper deposit in Yunnan. Non-Ferr Met Des 31:23–26 ((in Chinese with English abstract))

Zhang ZC, Hou T, Cheng ZG (2022) Mineralization related to Large Igneous Province. Acta Geol Sin 96:131–154 ((in Chinese with English abstract))

Zhao GC, Cawood PA (2012) Precambrian geology of China. Precambrian Res 222–223:13–54

Zhao JH, Li QW, Liu H, Wang W (2018) Neoproterozoic magmatism in the western and northern margins of the Yangtze Block (South China) controlled by slab subduction and subduction-transform-edge-propagator. Earth-Sci Rev 187:1–18

Zhao XF, Zhou MF (2011) Fe-Cu deposits in the Kangdian region, SW China: a Proterozoic IOCG (iron-oxide-copper-gold) metallogenic province. Miner Deposita 46:731–747

Zhao XF, Zhou MF, Li JW, Selby D, Li XH, Qi L (2013) Sulfide Re-Os and Rb-Sr isotope dating of the Kangdian IOCG metallogenic province, Southwest China: Implications for regional metallogenesis. Econ Geol 108:1489–1498

Zhao XF, Zhou MF, Su ZK, Li XC, Chen WT, Li JW (2017) Geology, geochronology, and geochemistry of the Dahongshan Fe-Cu-(Au-Ag) deposit, southwest China: Implications for the formation of iron oxide copper-gold deposits in intracratonic settings. Econ Geol 112:603–628

Zheng YF, Fu B, Li YL, Xiao YL, Li SG (1998) Oxygen and hydrogen isotope geochemistry of ultrahigh-pressure eclogites from the Dabie Mountains and the Sulu terrane. Earth Planet Sci Lett 155:113–129

Zheng YF, Fu B, Xiao YL, Li YL, Gong B (1999) Hydrogen and oxygen isotope evidence for fluid-rock interactions in the stages of pre- and post-UHP metamorphism in the Dabie Mountains. Lithos 46:677–693

Zheng YF, Chen JF (2000) Stable isotope geochemistry. Beijing, Science Press, 219 (in Chinese)

Zhou MF, Chen WT, Wang CY, Prevec SA, Liu PP, Howarth GH (2013) Two stages of immiscible liquid separation in the formation of Panzhihua-type Fe-Ti-V oxide deposits, SW China. Geosci Front 4:481–502

Zhou MF, Zhao XF, Chen WT, Li XC, Wang W, Yan DP, Qiu HN (2014) Proterozoic Fe-Cu metallogeny and suppercontinental cycles of the southwestern Yangtze Block, southern China and northern Vietnam. Earth-Sci Rev 139:59–82